POLITECNICO DI TORINO

Master's Degree
in Aerospace Engineering and Astronautics

Master's Thesis

Modelling of the upstream propagation of coastal surface waves into open channels

Application to the dynamics of undulating bores

Academic tutor:
Daniela TORDELLA (DISAT)

Student:
Beatrice BATTISTI

A. A. 2017/2018

Abstract

When long waves propagate into shallow water, their dynamics changes and an undular bore may generate. This undular motion is strictly dependent on the shape of the channel in which the waves are travelling. The code developped in the CARDAMOM team at Inria makes use of a two-dimensional, depth-averaged model which accounts for non-linear and dispersive effects for waves in shallow water.
First the code is used to simulate and compare the flow in a rectangular and in a trapezoidal channel. The presence of sloping banks triggers different dynamics along the cross-section of the channel and a transition of the wavelength for a certain Froude number Fr_{t_1} is observed. The simulation results are validated against experimental data.
As a proof of concept, we then vary the inclination of the banks of the trapezoidal channel in order to analyse its influence on Fr_{t_1}. As the numerical results show, a smaller banks slope induces longer waves and the transition takes place at higher Froude numbers.
The linearized theory for long waves proposed in [Chassagne, 2017] is endorsed for gently sloping banks channels.

Keywords: Surface waves, undular bore, Boussinesq-type model, Green-Naghdi equations, Shallow Water equations.

Contents

List of Figures

Introduction

An ocean wave is a perturbation that propagates in time and space along the interface between two different media: water and air. There are many kinds of surface waves, depending on the forces acting on them: gravity, surface tension, atmospheric pressure. The effect of these different forces is reflected on the wave period (Figure 1).

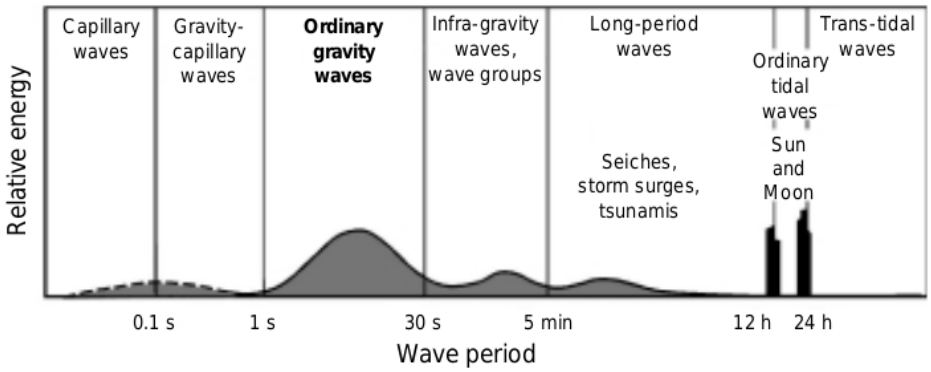

Figure 1 – Classification of ocean waves by wave period. Figure from [Laing, 1998].

A wave can be characterised by many quantities. Some of them are displayed in Figure 2.

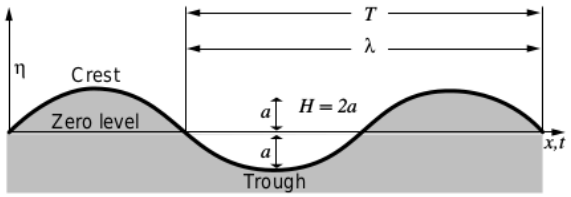

Figure 2 – Main characteristics of a simple surface wave. Figure from [Laing, 1998].

First of all, the shape of the wave is delineated by the free surface elevation $\eta = \eta(\mathbf{x}, t)$, where $\mathbf{x}$ is the vector of the spatial domain. The form of η allows to identify the *wave period* T, which is the time interval taken by successive wave crests to pass a fixed point. The period is linked to the *frequency* $f = 1/T$, i.e. the number of crests passing a fixed point in 1 second. In space, the *wavelength* λ represents the horizontal distance between two successive crests and the *amplitude* a is the maximum of the displacement from the mean sea-level.
A single wave advances at a certain speed, the *rate of propagation* c_ϕ or also *phase*

speed, which links the wavelength and the period through the relation $\lambda = c_\phi T$. When the individual wave is part of a train of waves, one must differentiate the phase speed from the *group speed*: the latter is the velocity of the entire wave envelope and of the wave energy too. Furthermore, we can define the *wavenumber* as $k = 2\pi/\lambda$ and the *angular frequency* as $\omega = 2\pi/T$. The wave speed results thus also as $c_\phi = \omega/k$ and the group speed is $c_g = \partial\omega/\partial k$.
Lastly, the variation of the phase speed with the wavelength is called *dispersion relation* and it is usually parametrised via the *dispersion parameter* $\mu = h_0/\lambda$. Note that $\frac{\mu}{2\pi} = kh_0$. The dispersion parameter, together with the *non-linearity parameter* $\epsilon = a/h_0$, plays a major role in the choice of the physical model used to describe waves dynamics.

In this study we focus on waves forming a *bore*. A bore can be defined as an hydraulic jump in translation, a discontinuity between two states of the fluid, with different speed and height, as in Figure 3.

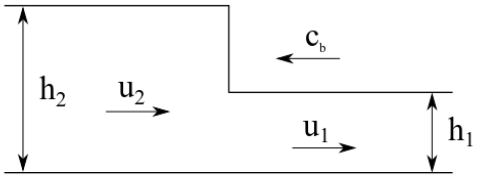

Figure 3 – Sketch of an hydraulic jump and definition of the main variables

It is common practice to define a fluid flow and its characteristics by a dimensionless number; using the variables of Figure 3, the *Froude number* is defined as follows

$$Fr = \frac{|u_1 - c_b|}{\sqrt{gh_1}}$$

where c_b is the *bore celerity*. The Froude number, in analogy to the Mach number for air flows, is the ratio of the inertia force to the weight of the fluid. For $Fr < 1$, the flow is subcritical, slow and with no waves. We concentrate on the dynamics of the supercritical flow, for the range $Fr > 1$.

As waves travel, all the water particles are affected, from the free surface to the bottom. However, when the water depth h_0 is big enough, the influence of the bottom can be neglected. In particular, we can distinguish between a *deep water* domain when $h_0 > \lambda/4$, and a *shallow water* regime when $h_0 < \lambda/25$. The transition between the two regions is for a *transitional depth*, where $\lambda/25 < h_0 < \lambda/4$ ([Laing, 1998]).
For example, water close to the shoreline is called shallow since the wavelength is considerably larger than the water depth; the entire ocean can be considered shallow as well because, there, the waves are in general extremely long. In both cases, we can say that μ is small.

Nearly all the characteristics of the waves change within the different zones: when the wave propagates from deep water to shallow water, only the period remains

constant. The wave speed and the wavelength decrease when h_0 decreases, while the wave height increases because of the conservation of the energy.

Tsunamis are waves characterised by very long wavelengths. They are nearly undetectable out in the ocean, but extremely dangerous when reaching the coast. Moreover, they are highly unpredictable and generated by large displacements of water. Their origin can be, among others, tectonics, earthquakes, landslides or underwater explosions.

For tsunami propagation, the shallow water hypothesis can be made, since μ is small. It is, in a first approximation, a non-dispersive phenomenon; however, although dispersion is small, it is present. When the motion takes place over a long time, dispersive effects may accumulate and eventually become non-negligible close to the coast.

It has been observed that short waves, such as undular bores and solitons, are generated by a long tsunami wave propagating into shallow water. The same behaviour can be seen when tides propagate into estuaries: long waves travelling upstream into shallow water undergo a progressive distorsion and generate tidal bores. As [Bonneton et al., 2015] have shown experimentally in the Gironde/Garonne estuary (France), tidal waves propagate long time upstream before forming a tidal bore, the onset position of which is difficult to determine and locate precisely.
This phenomenon is surely less alarming than a tsunami; it is anyhow important to understand it, since the secondary, undular waves created by the bore induce an amplitude growth of about half the amplitude of the primary wave. Neglecting this aspect when planning the height of the river walls would increase the risk of flooding, letting water overflow into residential areas at the riverside. Moreover, in rivers, the dynamics of these bores is exactly the same as that of tsunami-generated ones.

Field measurements are extemely difficult to carry out and only few records are available. During 2010 and 2011, [Bonneton et al., 2015] realized a big campaign in the Gironde/Garonne and in the Seine estuaries (France), for different times of the year, so as to encounter various tidal amplitudes and freshwater discharges.
Observations from more than 200 tides in rivers with sloping banks show a transition between different regimes around a Froude number Fr_{t_1} of about 1.10: an undular motion appears in addition to the main bore. The transition is visible also in the wavelength evolution, as shown in Figure 4.

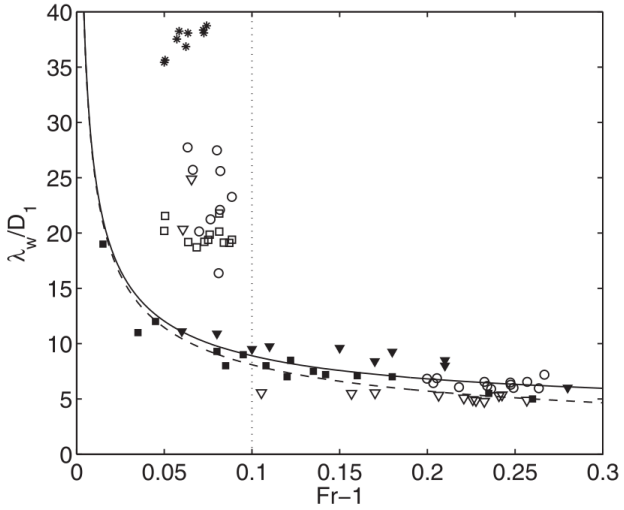

Figure 4 – Non-dimensional wavelength as a function of the Froude number minus 1. Square, circle, triangle: Garonne campaigns; asterisk: Seine campaign; solid square: experimental data by [Treske, 1994]; solid triangle: experimental data by [Favre, 1935]. Continuous line: theory by [Lemoine, 1948]; dashed line: approximate equation by [Bonneton et al., 2015]; dotted line: transition around $Fr \simeq 1.10$. Figure from [Bonneton et al., 2015].

For $Fr > Fr_{t_1}$, field results are in good agreement with laboratory data and theory's predictions; for smaller Froude numbers, instead, the wavelengths measured along the axis of the estuaries are much larger than those from the other sources. The same evolution is seen for the wave steepness.
This outcome goes along with that observed by Treske during his laboratory experiences [Treske, 1994]. Indeed, Treske found a great difference in the fluid behaviour on the axis of a trapezoidal channel with respect to a rectangular channel when passing a transition Froude number of $Fr_{t_1} = 1.15$. The value for Fr_{t_1} may be different from Bonneton but is very close: surely the gap is caused by the different experimental conditions, one carried out in real estuaries and the other in a laboratory, by mean of a manmade open channel. What is striking is that something is going on around a certain Fr_{t_1}.

Actually, another transition can be seen for all shapes of channels, at about $Fr_{t_2} = 1.30$: for very large Froude numbers, all the energy is dissipated by the turbulence. The bore is breaking, no secondary waves can be detected, leaving a simple translating hydraulic jump.

The different flow regimes can be resumed as in Figure 5.

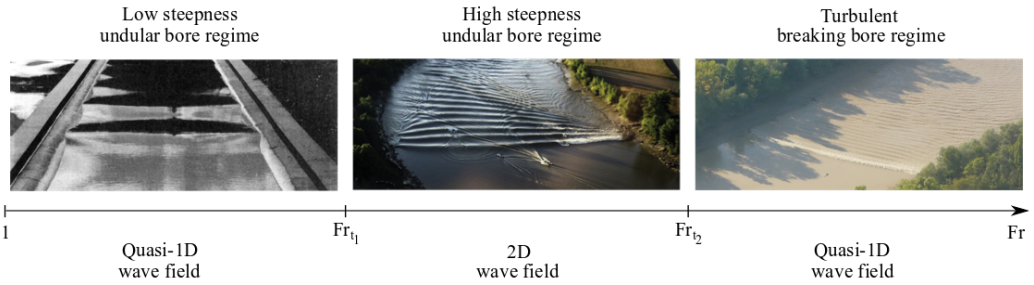

Figure 5 – Bore regimes according to the Froude number

Following the experiments of Treske, this work is focused on a flow travelling in a trapezoidal open channel, in the proximity of the first transition, i.e. around Fr_{t_1}, when the secondary wavefield appears. The flow dynamics is studied, especially its interaction with the sloping banks. In order to do so, a code developed in the CARDAMOM team to model shallow water flows in open channels is used.
The results of the numerical simulations allow us to observe how the interaction of the fluid with the gently sloping banks affect the transition. Moreover, they are used to validate the linearized theory developped in the CARDAMOM team for the prediction of the evolution of the wavelength with the Froude number in sloping banks channels.

The computational domain is a constant cross-section channel with regular banks and a simplified, symmetric trapezoidal bed. Such an approximation can be done to keep the computation easy to handle without loss of generality: long, smoothly changing estauries and rivers might be represented as a series of many shorter, regular channels.

In chapter 1 the equations governing the flow dynamics and the physical models used for shallow water problems are reviewed. In chapter 2 the numerical methods implemented in the code are described. Simulations are done firstly to validate the code and a previous work on the different flow dynamics in rectangular and trapezoidal channels (chapter 3); then, chapter 4 presents the analysis of the influence of the sloping banks on the flow field.

Chapter 1

Physical Models

Even though the two-phase (water-air) Navier-Stokes equations can describe in the most complete way the motion of the fluid in an open channel, they are excessively costly from a numerical point of view. Some assumptions can thus be made to simplify the model, while preserving a sufficient amount of physical informations. First of all, water is a Newtonian fluid and it is also incompressible, so the density ρ is kept constant. Moreover, for all applications only involving wave propagation, water can be considered inviscid: the Reynolds number goes to infinity. This hypothesis allows to prove the irrotationality of the fluid flow. As a consequence, velocity can be derived from a scalar potential. Furthermore, as the viscosity is neglected, the only forces acting on a water particle are gravity and pressure. For the scales used here, friction and surface tension can be ignored too. The Navier-Stokes equations are then simplified to the incompressible Euler equations with a moving boundary: the free surface.

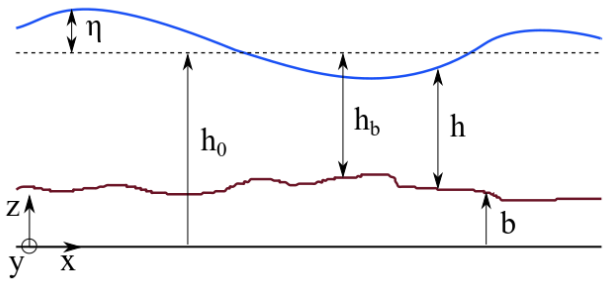

Figure 1.1 – Visual description of the free surface flow problem, with the main parameters.

In Figure 1.1 we can see the setting of the problem. It is a three-dimensional problem in the Cartesian coordinate system (x, y, z), but it can be reduced to a bi-dimensional one, in this case in the plane (x, z) for a lighter notation.
The velocity vector is denoted by $\mathbf{u} = (u, w)^T$; $\eta(x, t)$ is the free surface elevation, taken with respect to the water depth at rest h_0; $b(x)$ is the bathymetry, considered indipendent from time.

Taking into account all the hypotheses made so far, the Euler system of equations can be written as:

$$u_t + u\ u_x + w\ u_z + \frac{p_x}{\rho} = 0 \tag{1.1}$$

$$w_t + u\ w_x + w\ w_z + \frac{p_z}{\rho} + g = 0 \tag{1.2}$$

$$u_x + w_z = 0 \tag{1.3}$$

where p is the pressure, g is the gravity and the subscripts denote partial differentiation.

We recognise the two components of the momentum conservation (equations (1.1) and (1.2)), written in convective form, and the continuity equation (1.3), expressing incompressibility. The irrotationality condition can be added to the system:

$$u_z - w_x = 0 \tag{1.4}$$

This system is valid for $z \in [b(x), h_0 + \eta(x,t)]$, but in order to have a well-posed problem, we still have to add the boundary conditions at the free surface and at the bed.
Concerning the velocity boundary conditions, we define the free surface as $f(x,z,t) = z - (h_0 + \eta(x,t))$ and knowing that the interface water-air is immiscible, so that the normal component of the velocity must be the same in the two fluids, we get the first boundary condition:

$$w = \eta_t + u\ \eta_x \qquad \text{at} \quad z = h_0 + \eta(x,t) \tag{1.5}$$

The slip-wall condition at the bed can be derived following the same procedure:

$$w = u\ b_x \qquad \text{at} \quad z = b(x) \tag{1.6}$$

As for the pressure at the free surface, we consider that it is constant across the interface: $p = p_{atm}$ at $z = h_0 + \eta(x,t)$. The boundary condition is thus given by the Bernoulli's equation applied at the free surface with a suitable choice of the integration constant, equal to p_{atm}.

1.1 Asymptotic Development

Large scale simulations using the Euler equations are still prohibitive in term of computational cost, essentially due to their 3D nature. For this reason, other models have been developed, leading to the Boussinesq approach. [Boussinesq, 1872] was the first one to propose, for shallow water flows, a depth-averaged system of equations in which the velocity is expressed by an asymptotic development with respect to a depth-averaged velocity $\bar{u}$. The degree of approximation of the equations is controlled by two non-dimensional parameters referring to the physics of the problem: the non-linearity of the flow ϵ and the dispersion of the waves μ.

Before applying the simplifications, we need to rewrite the Euler system without the pressure term. From equations (1.1) to (1.6), using the pressure boundary conditions on the free surface, we obtain:

$$
\begin{aligned}
u_t(h_0+\eta)+\eta_x w_t(h_0+\eta)+g\eta_x+\left[\frac{u^2(h_0+\eta)}{2}\right]_x+\left[\frac{w^2(h_0+\eta)}{2}\right]_x&=0\\
u_x+w_z&=0\\
u_z-w_x&=0\\
w=\eta_t+u\ \eta_x \qquad &\text{at}\quad z=h_0+\eta(x,t)\\
w=u\ b_x \qquad &\text{at}\quad z=b(x)
\end{aligned}
\tag{1.7}
$$

Now, let the dimensionless variables be introduced as follows:

$$
x'=\frac{x}{\lambda}\quad z'=\frac{z}{h_0}\quad t'=\frac{\sqrt{gh_0}}{\lambda}t\quad \eta'=\frac{\eta}{a}\quad b'=\frac{b}{h_0}
$$

$$
u'=\frac{h_0}{a\sqrt{gh_0}}u\quad w'=\frac{\lambda}{a}\frac{1}{\sqrt{gh_0}}w\quad p'=\frac{p}{gh_0\rho}
$$

Dropping the primes for sake of clarity, we riformulate system (1.7) in a dimensionless form:

$$
\begin{aligned}
u_t(1+\epsilon\eta)+\epsilon\mu^2\eta_x w_t(1+\epsilon\eta)+\eta_x+\epsilon\left[\frac{u^2(1+\epsilon\eta)}{2}\right]_x+\epsilon\mu^2\left[\frac{w^2(1+\epsilon\eta)}{2}\right]_x&=0\\
u_x+w_z&=0\\
u_z-\mu^2 w_x&=0\\
w=\eta_t+\epsilon u\ \eta_x \qquad &\text{at}\quad z=1+\epsilon\eta\\
w=u\ b_x \qquad &\text{at}\quad z=b
\end{aligned}
\tag{1.8}
$$

Combining the second and third equations of (1.8) and after some manipulations, we are able to express the horizontal velocity at an arbritrary level $\tilde{u}$ as an asymptotic development of the depth-averaged horizontal velocity $\bar{u}=\frac{1}{(1+\epsilon\eta-b)}\int_b^{1+\epsilon\eta}u\,dz$. The resulting expression is

$$
\begin{aligned}
\tilde{u}=\bar{u}-\mu^2\Bigg[&\left(\frac{(\tilde{z}-1)^2}{2}-\frac{h^2}{6}+\frac{h_b}{2}(h-h_b)\right)\bar{u}_{xx}+\\
&+\left((\tilde{z}-1)-\left(\frac{h}{2}-h_b\right)\right)(h_b\bar{u})_{xx}\Bigg]+\mathcal{O}(\mu^4)
\end{aligned}
\tag{1.9}
$$

The expression for the asymptotic development of the vertical velocity can be found as well as

$$
\tilde{w}=-\left((\tilde{z}-1)\bar{u}_x+(h_b\bar{u})_x\right)+\mathcal{O}(\mu^2) \tag{1.10}
$$

The different Boussinesq-type («BT») models that have been developed are based on the choice of a certain order of truncature for the asymptotic development of the velocities.

1.2 Non-Linear Shallow Water equations

The simplest and most used model is based on the assumption that:

$$\mathcal{O}(\epsilon) \sim 1 \qquad \text{and} \qquad \mathcal{O}(\mu^2) \ll 1$$

Thus the velocity (1.9) reduces to

$$\tilde{u} = \bar{u} + \mathcal{O}(\mu^2)$$

Substituting this relation in the first equation of (1.8), coupling it with the continuity equation and coming back to physical variables allows us to finally obtain the following system:

$$\begin{aligned} \eta_t + (h\bar{u})_x &= 0 \\ \bar{u}_t + \bar{u}\bar{u}_x + g\eta_x &= 0 \end{aligned} \tag{1.11}$$

In two-dimensions, system (1.11) reads:

$$\begin{aligned} \eta_t + \nabla \cdot (h\bar{\mathbf{u}}) &= 0 \\ \bar{\mathbf{u}}_t + (\bar{\mathbf{u}} \cdot \nabla)\bar{\mathbf{u}} + g\nabla\eta &= 0 \end{aligned} \tag{1.12}$$

For numerical purposes, the most suitable form for this system is the conservative one: introducing the new variable $\bar{\mathbf{q}} = h\bar{\mathbf{u}}$ of the volume flux, we finally obtain

$$\begin{aligned} h_t + \nabla \cdot \bar{\mathbf{q}} &= 0 \\ \bar{\mathbf{q}}_t + \nabla \cdot \left(\frac{\bar{\mathbf{q}} \otimes \bar{\mathbf{q}}}{h} \right) + \nabla \left(\frac{gh^2}{2} \right) + gh\nabla h_b &= 0 \end{aligned} \tag{1.13}$$

We can see that the Non-Linear Shallow Water («NLSW») system is composed of non-linear hyperbolic partial differential equations plus a source term ($gh\nabla h_b$) modelling the effects of the topography. Hyperbolicity implies that the solutions may evolve discontinuities. Physically speaking, these discontinuities can be seen as breaking waves.
It must be noticed too that there is no dispersion in the NLSW model: in fact dispersion properties arise from the presence of third order derivatives, here absent since they are of order $\mathcal{O}(\mu^2)$.

In general, a model can be characterized by the phase velocity. The expression for c_ϕ is obtained by doing a Fourier analysis of the linearized system, looking for a solution in the form $\eta(x,t) = \eta_0 \exp^{\nu t - ikx}$ and $\bar{u}(x,t) = \bar{u}_0 \exp^{\nu t - ikx}$, where $\nu = \zeta + i\omega$, with ζ being the *dissipation rate* and ω the *phase shift*.

Solving the 1D linearized system with the expressions just mentioned, one obtains

$$\begin{aligned} \zeta &= 0 \\ \omega^2 &= k^2 g h_0 \end{aligned}$$

Using the definition $c_\phi = \omega/k$, we can see that the phase velocity of the waves is indipendent of the wavenumber: each wave will travel with the same speed $c_\phi^2 = gh_0$. This is the main reason why the NLSW is valid for shallow water problems, where the parameter μ is very small, but it is not suitable for regions in which the dispersion is important, as in intermediate waters.

1.3 Dispersive Non-Linear BT equations

Improvements of the NSLW system can be done by considering higher orders in the asymptotic development. In this way, dispersion is introduced in the equations and allows to describe more general problems.

1.3.1 Weakly Dispersive Weakly Non-Linear BT Equations

Weakly dispersive and weakly non-linear BT models are obtained by adding to the NLSW equations a perturbation computed under the hypothesis that

$$\epsilon \ll 1,\ \mu^2 \ll 1 \qquad \text{and} \qquad \epsilon = \mathcal{O}(\mu^2)\ .$$

In this case, we obtain a first set of equations, starting from the Euler system, in which all the $\mathcal{O}(\epsilon)$ and $\mathcal{O}(\mu^2)$ terms are considered and the $\mathcal{O}(\epsilon\mu^2)$ and $\mathcal{O}(\mu^4)$ are neglected. The resulting system is composed of an hyperbolic part, as for the NLSW system, together with additional terms, accounting for the higher order dispersive terms.

Many models obtained with the aforementioned hypothesis have been proposed by, among others, [Peregrine, 1966], [Beji and Nadaoka, 1996], [Madsen and Sørensen, 1992], [Nwogu, 1993].

The Peregrine model

Peregrine obtained his Boussinesq-type model neglecting the terms of order $\mathcal{O}(\epsilon\mu^2)$ in the asymptotic development (1.9) and the system of equations reads as ([Peregrine, 1966])

$$\begin{gathered} \eta_t + (h\bar{u})_x = 0 \\ \bar{u}_t + \bar{u}\bar{u}_x + g\eta_x + \tfrac{h_b^2}{6}\bar{u}_{xxt} - \tfrac{h_b}{2}(h_b\bar{u})_{xxt} = 0 \end{gathered} \tag{1.14}$$

and in a conservative form:

$$\begin{gathered} h_t + (h\bar{q})_x = 0 \\ \bar{q}_t + \left(\tfrac{\bar{q}^2}{h}\right)_x + gh\eta_x + hP_t(\bar{u}) = 0 \end{gathered} \tag{1.15}$$

where we define the elliptic operator

$$P(\cdot) = \frac{h_b^2}{6}(\cdot)_{xx} - \frac{h_b}{2}(h_b(\cdot))_{xx} \tag{1.16}$$

The two-dimensional form can be easily derived. The Fourier analysis gives, in this case, a phase velocity depending on the wavenumber:

$$c_\phi^2 = \frac{gh_0}{1 + \frac{(kh_0)^2}{3}} \tag{1.17}$$

The Madsen-Sørensen model

Madsen and Sørensen improved the linear dispersion and the shoaling properties of the Peregrine model obtaining a more complex structure as follows ([Madsen and Sørensen, 1992]):

$$\begin{gathered} h_t + (h\bar{q})_x = 0 \\ \bar{q}_t + \left(\frac{\bar{q}^2}{h}\right)_x + gh\eta_x - h\tilde{P}_t(\bar{u}) - g\beta h\hat{P}(\eta_x) = 0 \end{gathered} \tag{1.18}$$

where

$$\tilde{P}(\cdot) = \left(\frac{1}{3} + \beta\right) h_b^2(\cdot)_{xx} + (1 + 2\beta)h_b(h_b)_x(\cdot)_x \tag{1.19}$$

and

$$\hat{P}(\cdot) = h_b^2(\cdot)_{xx} + 2h_b(h_b)_x(\cdot)_x \tag{1.20}$$

The Peregrine system can be found when putting the tuning parameter $\beta = 0$. The phase velocity is now

$$c_\phi^2 = gh_0 \frac{1 + \beta(kh_0)^2}{1 + \left(\frac{1}{3} + \beta\right)(kh_0)^2} \tag{1.21}$$

If we compare the linear phase error (Figure 1.2) of the NLSW, the Peregrine (here called «P-A», where A stands for Abbott, who slightly modified Peregrine's model while keeping all the linear properties of the original) and the Madsen-Sørensen (here «MS») models, we can see that the latter, with $\beta = 1/15$, gives an error less than 2% in almost all range of kh_0 considered. The comparison is made with respect to the phase velocity computed using the Airy wave theory, which is derived from the linearisation of the Euler equations.

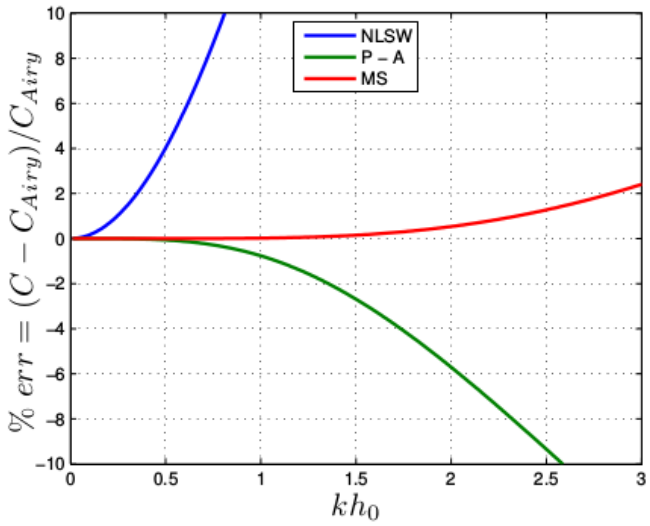

Figure 1.2 – Percentage error in the phase velocity description with respect to the Airy wave theory for the weakly non-linear models. From [Filippini, 2016].

The Korteweg - de Vries Equation

A simpler variant of these weakly non-linear dispersive models is the Korteweg - de Vries equation. This model consists of a one-dimensional non-linear partial differential equation of third order.
The starting point of the work done by Korteweg and de Vries is the same as that of Boussinesq: the Rayleigh's series expansion for the wave velocity[†]. In both cases, they consider an incompressible, rotation-free, frictionless fluid.
The two theories for long waves in shallow water were formulated separately at the end of the 19th century. Their result is quite similar, nevertheless they are different. One of the differences concerns, for example, the frame of reference: while Boussinesq used a fixed coordinate system, Korteweg and de Vries used a coordinate system moving with the wave. We can thus define the following variables:

$$\eta(x,t) = \zeta(\tau,x)Q(x) \qquad Q(x) = \left[\frac{h}{h_0}\right]^{-\frac{1}{4}}$$
$$\tau = t - \int \frac{dx}{c(x)} \qquad c(x) = \sqrt{gh(x)}$$

Furthermore, unlike Boussinesq, the KdV theory is centered on only one equation ([Grue et al., 2008]):

$$\frac{\partial\zeta}{\partial x} - \frac{3\zeta Q(x)}{2h(x)c(x)}\frac{\partial\zeta}{\partial\tau} - \frac{h^2(x)}{6c^3(x)}\frac{\partial^3\zeta}{\partial\tau^3} = 0 \tag{1.22}$$

We refer to [de Jager, 2006] and the references therein for an extensive review.

The KdV model has some interest because it accounts for non-linearity and dispersion. Moreover, approximation wouldn't be needed because the analitical solution of the KdV equation would give a more precise idea of the flow dynamics. However, [Grue et al., 2008] showed some non-negligible limits of the KdV model.

In the context of the Indian Ocean Tsunami, Grue compared this model to the BT model by Peregrine: both models show the formation of short waves, but the former exhibits some severe shortcomings with respect to the latter. Indeed, the KdV model predicts unrealistically large wave peaks and a wider wave spectrum than the Peregrine model. Therefore, even if the KdV model could give a more accurate solution, it poorly resolves the short waves in the first place. Moreover, it is well established for 1D problems, which are a too strong restriction. As an example, the flow field studied here is fully bidimensional.

1.3.2 Weakly Dispersive Fully Non-Linear BT Equations

Broadly speaking, when approaching very shallow water, the domain goes well outside the range of weakly non-linear models: the effects of the non-linearity become too strong and we need a model which can handle them, along with the dispersion. This is the reason why fully non-linear models are necessary.

In this case, the range of validity is enhanced to

[†]L. Rayleigh, On Waves, *The London, Edinburgh, and Dublin Philosophical Magazine and Journal of Science*, 4:257-279, 1876.

$$\epsilon \sim \mathcal{O}(1) \qquad \text{and} \qquad \mu^2 \ll 1$$

where the former represents the non-linearity and the latter the weakly dispersive character of the model.

[Green and Naghdi, 1976] derived a set of equations in which the velocity is expressed as:

$$u(1+\epsilon\eta) = \bar{u} - \mu^2 \left(\left(\frac{h^2}{3} - \frac{h h_b}{2} \right) \bar{u}_{xx} + \frac{h}{2} \left(h_b \bar{u} \right)_{xx} \right) + \mathcal{O}(\mu^4) \tag{1.23}$$

and

$$w(1+\epsilon\eta) = -\left((h - h_b)\bar{u}_x + (h_b \bar{u})_x \right) + \mathcal{O}(\mu^2) \tag{1.24}$$

Substituting (1.23) and (1.24) in the first equation of system (1.8), we get an expression for the momentum equation; this is then coupled with the continuity equation to give, in dimensional form:

$$\begin{aligned} \eta_t + (h\bar{u})_x &= 0 \\ (1+\mathcal{T})(\bar{u}_t + \bar{u}\bar{u}_x) + g\eta_x + \mathcal{Q}_1(\bar{u}) &= 0 \end{aligned} \tag{1.25}$$

with

$$\mathcal{T}(\cdot) = -\frac{1}{3h} \left(h^3 (\cdot)_x \right)_x - \frac{h}{2} (\cdot)_x b_x + \frac{1}{2h} \left(h^2 b_x (\cdot) \right)_x + b_x (\cdot) b_x \tag{1.26}$$

$$\mathcal{Q}_1(\cdot) = -\frac{2}{3h} \left(h^3 \left((\cdot)_x \right)^2 \right)_x + h \left((\cdot)_x \right)^2 b_x + \frac{1}{2h} \left(h^2 (\cdot)^2 b_{xx} \right)_x + (\cdot)^2 b_{xx} b_x \tag{1.27}$$

In a two-dimensional, conservative form we have:

$$\begin{aligned} h_t + \nabla \cdot (h\bar{\mathbf{u}}) &= 0 \\ (\mathbb{I} + \alpha\mathbb{T}) \left(\bar{\mathbf{q}}_t + \nabla \cdot \left(\frac{\bar{\mathbf{q}} \otimes \bar{\mathbf{q}}}{h} \right) + g \frac{\alpha - 1}{\alpha} h \nabla\eta \right) + \frac{g}{\alpha} h \nabla\eta + h\mathbb{Q}_1(\bar{\mathbf{u}}) &= 0 \end{aligned} \tag{1.28}$$

with $\mathbb{I}$ as the unit matrix, and the two operators $\mathbb{T}$ and $\mathbb{Q}_1$ containing second and third derivatives, respectively:

$$\begin{aligned} \mathbb{T}(\cdot) = &-\frac{1}{3} \nabla \left(h^3 \nabla \cdot \left(\frac{(\cdot)}{h} \right) \right) - \frac{h^2}{2} \left(\nabla \cdot \left(\frac{(\cdot)}{h} \right) \right) \nabla b + \\ &+ \frac{1}{2} \nabla \left(h^2 \nabla b \cdot \left(\frac{(\cdot)}{h} \right) \right) + h \left(\nabla b \cdot \left(\frac{(\cdot)}{h} \right) \right) \nabla b \end{aligned} \tag{1.29}$$

$$\begin{aligned} \mathbb{Q}_1(\cdot) = &-\frac{2}{3h} \nabla \left(h^3 \left(\nabla (\cdot)_1 \cdot \nabla^\perp (\cdot)_2 + (\nabla \cdot (\cdot))^2 \right) \right) + \\ &+ h^2 \left(\nabla (\cdot)_1 \cdot \nabla^\perp (\cdot)_2 + (\nabla \cdot (\cdot))^2 \right) \nabla b + \\ &+ \frac{1}{2h} \nabla \left(h^2 \left((\cdot) \cdot \left((\cdot) \cdot \nabla \right) \nabla b \right) \right) + \\ &+ \left((\cdot) \cdot \left((\cdot) \cdot \nabla \right) \nabla b \right) \nabla b \end{aligned} \tag{1.30}$$

It must be noticed the presence of a tuning parameter α in equation (1.28). This form has been proposed by [Chazel et al., 2011]. According to Chazel, α is used to enhance linear frequency dispersion and shoaling properties, giving the so-called *eGN (enhanced GN system)*. It is possible to recover the original Green-Naghdi («GN») model simply putting $\alpha = 1$.

The GN system contains third order derivatives of the type $(\cdot)_{xxt}$ or $(\cdot)_{xxx}$, which imply, in the Fourier analysis, a dependence of the group velocity with respect to the wavenumber:

$$c_\phi^2 = gh_0 \frac{1 + \left(\frac{\alpha-1}{3}\right)(kh_0)^2}{1 + \frac{\alpha}{3}(kh_0)^2} \tag{1.31}$$

Each wave thus travels at its own speed and this is the basic mechanism of dispersion. The form of (1.31) has a structure similar to that of the MS model. The value $\alpha = 1.159$ is suggested in [Chazel et al., 2011] as an optimal choice. We can see in Figure 1.3 that the error never exceeds 1% in absolute value, for the entire range of kh_0.

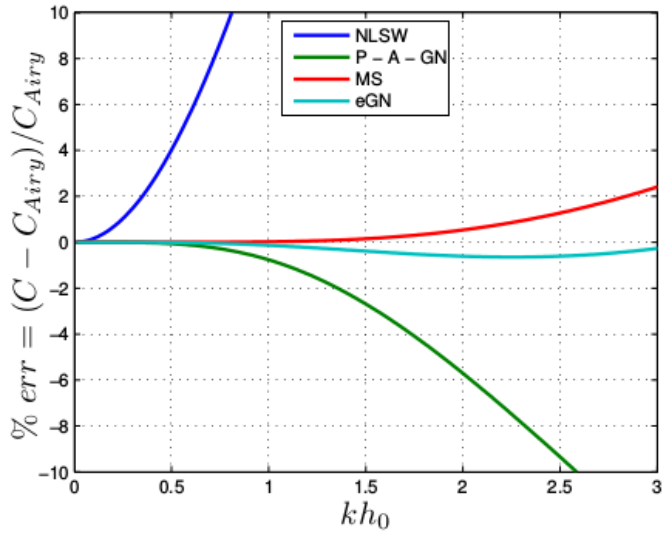

Figure 1.3 – Percentage error in the phase velocity description with respect to the Airy wave theory for the fully non-linear model. From [Filippini, 2016].

The weak point of the GN model, as all BT models, is the inability to account for wave breaking. All depth-averaged models are unable to simulate the breaking process and the consequent energy dissipation. It is thus necessary to add a condition in the models such that, if satisfied, it triggers an energy dissipation mechanism. The latter can, among other possibilities, be performed by the NLSW model, for it reproduces correctly the breaking process. This aspect is discussed in more details in section 2.

1.3.3 Qualitative Comparison of the Boussinesq-type Models

From an analytical point of view, it is now clear the difference between the NLSW system (or Saint-Venant equations) and the dispersive equations; we want to show this difference with a simple numerical example.

Defining a bore as a translating hydraulic jump, we define a discontinuity at a point x_0 close to the entry of a one-dimensional channel and we leave it travel for a certain length L_x.

Sufficiently far from the jump, assuming the overall conservation of mass and momentum, we can write the jump conditions, better known as the Rankine-Hugoniot equations, relating the flow conditions before and after the discontinuity. It can be shown that we obtain the following relations ([Ali and Kalisch, 2010]):

$$u_1 - c_b = \left(\frac{gh_2}{2h_1}(h_1 + h_2)\right)^{1/2} \tag{1.32}$$

$$u_2 - c_b = \left(\frac{gh_1}{2h_2}(h_1 + h_2)\right)^{1/2} \tag{1.33}$$

The parameters imposed are the water velocity and the upstream depth, u_1 and h_1; the bore strength, via the Froude number, is also chosen. Then, from the definition of the Froude number, the value of c_b can be obtained. From equation (1.32), h_2 is computed and finally equation (1.33) gives the value of u_2. All the variables are thus computed and the initial solution is completely defined as an hyperbolic tangent, smoothly joining the two states:

$$\begin{aligned} h(x, t = 0) &= \frac{h_2 - h_1}{2} \tanh\left(\frac{x - x_0}{l_t}\right) + h_2 \\ u(x, t = 0) &= \frac{u_2 - u_1}{2} \tanh\left(\frac{x - x_0}{l_t}\right) + u_2 \\ v(x, t = 0) &= 0 \end{aligned} \tag{1.34}$$

where l_t is the curvature of the hyperbolic tangent. The initial solution is visualized in Figure 1.4.

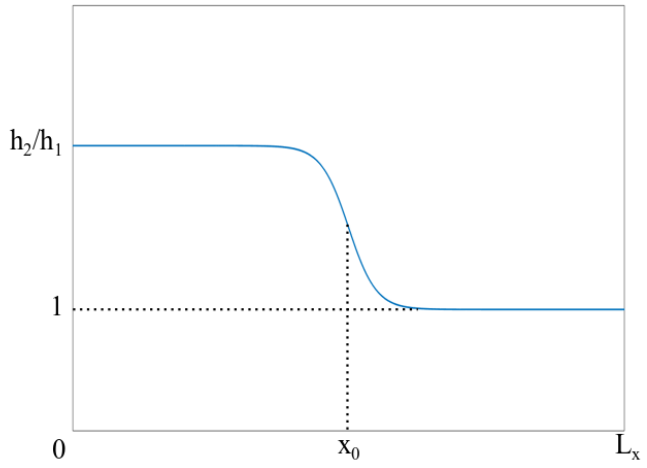

Figure 1.4 – Initial solution for the one-dimensional problem.

As mentioned before, the variables at the origin of the channel are imposed, so

$$\begin{aligned} h(x=0,t) &= h_1 \\ u(x=0,t) &= u_1 \\ v(x=0,t) &= 0 \end{aligned} \tag{1.35}$$

while for the exit, at $x = L_x$, the boundary conditions are obtained using the method of the characteristics: we want the perturbation to leave freely the domain.

So we put $h_1 = 1\,\mathrm{m}$ for simplicity and $u_1 = 0\,\mathrm{m/s}$; $Fr = 1.20$ is chosen in such a way as to be sure to see the undular motion developping. Here $x_0 = 0$ and the channel is extended 30 m on the left and 100 m on the right of the origin. The spatial discretization is taken as $\Delta x = 0.02$. Solutions are plotted every 5 seconds for both NLSW and GN models, superposed (Figure 1.5).

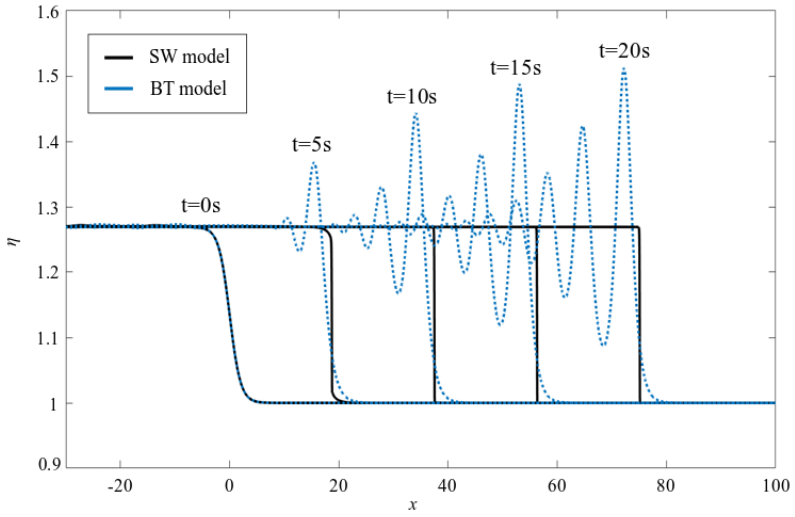

Figure 1.5 – Propagation of a tidal bore computed with NLSW and GN models.

The difference in the results is striking: while secondary waves appear immediately for the GN model, no sign of them is found for the NLSW model, which keeps transporting the jump and gradually transforms it into a sharp discontinuity. Furthermore, the amplitudes predicted by the two models disagree considerably: the secondary waves amplitude becomes very important as they keep going and it can eventually increase up to 1.5/2 times the constant amplitude of the jump.

1.4 Modelisation of Shoaling

When waves propagate into shallow water, the water depth gets smaller and smaller and the wave height gets bigger: this is called the *shoaling* effect. Entering zones of small depth induces the wavelength to reduce while frequency remains constant; also both phase velocity and group velocity change.

Let's take the energy balance: in absence of wave dissipation, the total transport of wave energy in the longitudinal direction is not affected so that, for stationary conditions, we have ([Laing, 1998])

$$\frac{d}{dx}\left(c_g E\right) = 0 \tag{1.36}$$

where $c_g E$ is the energy flux per unit crest length; precisely, $E = \rho g h^2/8$. It is evident that any decrease in c_g must be accompanied by a corresponding increase in wave height h in order to keep equation (1.36) true. This is the reason why waves elevation increases near shore, in a dramatic way when talking about highly energetic phenomena such as tsunamis.

In our case, we are keeping the bottom flat along x so we don't expect shoaling in that direction. Transversally, however, the presence of sloping banks will introduce some shoaling effect.

1.5 Energy Law for an Undular Bore

The energy argument is not important only for the shoaling effect. It is also at the origin of the generation of the secondary waves. We try to give a brief clarification of the physics behind it.

It is common knowledge that a sharp transition in both flow depth and flow velocity, which conserves both mass and momentum, necessitates a loss of energy across the discontinuity: this is what shallow water equations predict, as seen in Rayleigh[†].

This loss of energy across the bore front can be explained by pointing to the physical effects neglected by the shallow water theory, such as viscosity, frequency dispersion and turbulent flow. Actually, in strong bores, turbulent dissipation accounts for most of the energy dissipation, but in this work we are focusing on smaller Froude numbers, where turbulence has not developed yet. Moreover, bottom boundary layer and frictional effects are not considered in the bore model because it is originated from the Euler equations and not from the Navier-Stokes equations.

For weak bores, the inclusion of dispersive effects is indeed sufficient to explain the energy loss predicted by the NLSW system: physically, this is expressed by the creation of oscillations in the free surface behind the front.

We consider a control volume of unit width, bounded laterally by the sides of the interval $[x_1, x_2]$, where x_1 is far to the left of the bore front and x_2 is far to the right, and vertically by the free surface η and the bottom b.

We can write the total mechanical energy inside the control volume as the sum of the kinetic and the potential energy:

$$E = \int_{x_1}^{x_2} \int_{b}^{\eta} \left\{ \frac{\rho}{2}(u^2 + v^2) + \rho g z \right\} dz \; dx \tag{1.37}$$

[†]L. Rayleigh, On the Theory of Long Waves and Bores, *Proceedings of the Royal Society of London A: Mathematical, Physical and Engineering Sciences*, 90(619):324-328, 1914.

The conservation of energy is thus:

$$\frac{d}{dt}\int_{x_1}^{x_2}\int_b^\eta \left\{\frac{\rho}{2}(u^2+v^2)+\rho g z\right\} dz\, dx = \\ = \left[\int_b^\eta \left\{\left(\frac{\rho}{2}(u^2+v^2)+\rho g z\right)u + up\right\} dz\right]_{x_2}^{x_1} \quad (1.38)$$

Some manipulations can be done to equation (1.38) in the same way as done in sections 1.3.1 and 1.3.2. It can be shown that the non-dimensional energy balance results in

$$\frac{\partial \tilde{E}}{\partial \tilde{t}} + \frac{\partial \tilde{q}_E}{\partial \tilde{x}} = \mathcal{O}(\epsilon\mu^2) \quad (1.39)$$

Thus there is no energy loss in a dispersive system; numerical simulations confirm that the net energy flux agrees with the change in $\tilde{E}$ to the machine precision.

For an horizontal bed, we can express in dimensional form the energy density as

$$E = \frac{\rho g}{2}h^2 + \frac{\rho}{2}hu^2 + \frac{\rho}{6}h^3h_x^2 \quad (1.40)$$

and the energy flux, considering also the work rate due to pressure forces, as

$$q_E = \rho g u h^2 + \frac{\rho}{2}u^3 h - \frac{\rho}{3}h^3 u\left(u_{xt} + uu_{xx} - \frac{3}{2}u_x^2\right) \quad (1.41)$$

There is no exact conservation law connected with E: E approximates the energy of the full problem in the same way as the solution of a BT system approximates the solutions of the full surface water-wave problem.

A simplification of equations (1.40) and (1.41) for $\mu^2 \to 0$ can be done and the corresponding expressions for shallow water are derived:

$$E^{SW} = \frac{\rho g}{2}h^2 + \frac{\rho}{2}hu^2 \quad (1.42)$$

and

$$q_E^{SW} = \rho g u h^2 + \frac{\rho}{2}u^3 h \quad (1.43)$$

It is evident that $E^{SW} \neq E$ and $q_E^{SW} \neq q_E$.

Since we have taken x_1 and x_2 sufficiently far from the bore front, shallow water theory should be valid at those points. The usual formula for the energy loss in SW theory is

$$\frac{d}{dt}E^{SW} + \Delta q_E^{SW} = -\Lambda + \mathcal{O}(\mu^2) \quad (1.44)$$

with

$$\Lambda = \frac{\rho}{4}a_0^3\sqrt{\frac{1}{2}g^3\left(\frac{1}{h_0} + \frac{1}{h_0+a_0}\right)}$$

where a_0 is the bore amplitude and $\Delta q_E^{SW} = q_E^{SW}(x_2,t) - q_E^{SW}(x_1,t)$ represents the net influx of energy into the control volume. Λ is the energy loss due to the approximate nature of the governing Saint-Venant equations.
We can rewrite equation (1.39) in a way closer to equation (1.44): since $\epsilon\mu^2 \ll 1$,

$$\frac{d}{dt}E + \Delta q_E \simeq 0 \tag{1.45}$$

Adding and subtracting the NLSW terms to equation (1.45) gives:

$$\frac{d}{dt}E^{SW} + \frac{d}{dt}(E - E^{SW}) + \Delta q_E^{SW} + \Delta(q_E - q_E^{SW}) \simeq 0 \tag{1.46}$$

We introduce the differences $E^{NH} = E - E^{SW}$ and $q_E^{NH} = q_E - q_E^{SW}$, representing the non-hydrostatic («NH») terms. Using equation (1.44), equation (1.46) becomes:

$$\frac{d}{dt}E^{NH} + \Delta q_E^{NH} \simeq \Lambda \tag{1.47}$$

The energy which is lost in the discontinuity in the SW model is rather used by the non-hydrostatic part of the GN model for the creation of an undular bore: Λ gives an estimate of the amount of energy fed in the oscillatory motion of the free surface.

It must be noticed that we have considered the simplified case of a flat, horizontal bottom: bottom topography actually influences the distribution of energy and equations are more complicated when considering $b_x \neq 0$.

1.6 Physical Development of an Undular Bore

The creation of an undular bore is evident in nature and it has been justified analitically from an energetic point of view. It is now interesting to investigate the physical mechanism that triggers the undular motion behind the bore front.

We consider that an initially smooth positive wave steepens while travelling and undulations slowly grow at the front head. The undulations are not described by NLSW equations because the phenomenon is linked to non-hydrostatic pressure distribution near the bore front.

Consider a long shallow-water wave like that in Figure 1.6(a): its motion can be well described by Saint-Venant equations, as the change in water level is smooth enough and the pressure is effectively hydrostatic.
However, the wave celerity depends on the water depth: thus, point A travels faster than point E. While travelling, the wave therefore steepens until the water surface curvature becomes sufficiently important to affect the pressure distribution significantly. In this state, there is a downward pressure gradient beneath the surface which is greater than hydrostatic between point E and point C. Likewise, the downward pressure gradient between point A and point C is less than hydrostatic. Since points B and D are the points of maximum water surface curvature, they are also subject to the maximum change from hydrostatic pressure: the pressure beneath point D is greater than hydrostatic and beneath point B is less.

Those alterations affect also the horizontal pressure gradient (Figure 1.6(b)) among the different points; this results in additional horizontal currents and vertical displacements of the water surface. In particular, point B feels an extra

elevation while point D faces a corresponding depression; points A and E undergo the same phenomenon, but less intense, so that A is slightly lowered and E is slightly raised (Figure 1.6(c)). The process continues, a sequence of waves forms and grows in amplitude, until reaching an equilibrium or eventually breaking.

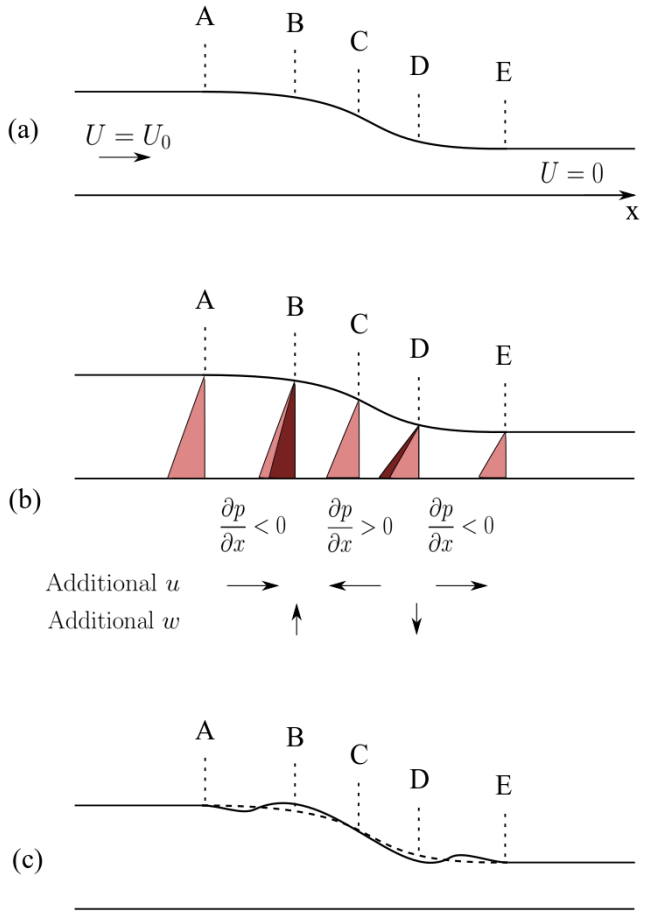

Figure 1.6 – The development of an undular bore. (a) The initial wave. (b) The extra horizontal pressure gradient. (c) The resulting free-surface deformation.

Completely developed undular bores have been classified by Favre according to their ratio of the change in the water level $\Delta\eta$ to the undisturbed water depth ([Favre, 1935]): undular bores are non-breaking when $\Delta\eta/h_0 < 0.28$, for $0.28 < \Delta\eta/h_0 < 0.75$ at least one of the leading waves of the undular bore is breaking and for greater differences there are no short waves, the bore is broken.

Chapter 2

Numerical Methods

Once the physical model has been chosen, it is necessary to solve it numerically. The choice is now diverted on the most appropriate numerical method needed to discretize the equations on a given mesh grid. The approach developed in the CARDAMOM team is based on a hybrid strategy, allowing to deal separately with the NLSW part and with the non-hydrostatic part.
We express here equations in one dimension for sake of simplicity, but the system which is actually solved is 2D.

Space Discretization

To appropriately discretize the equations, some manipulations are required.

Starting from system (1.25), and using the conservative variables (h, q), we can write the GN equations in this way:

$$\begin{gathered} h_t + q_x = 0 \\ (I + \alpha T)\left[q_t + \left(\frac{q^2}{h}\right)_x + gh\eta_x\right] - T(gh\eta_x) + h\mathcal{Q}_1(u) = 0 \end{gathered} \tag{2.1}$$

so that the operator $(I + \alpha T)$ is applied to the full shallow water momentum residual.
A splitting of (2.1) is now possible:

$$(I + \alpha T)\phi = \mathcal{W} - \mathcal{R} \tag{2.2}$$

$$\begin{gathered} h_t + q_x = 0 \\ q_t + \left(\frac{q^2}{h}\right)_x + gh\eta_x = \phi \end{gathered} \tag{2.3}$$

where $\mathcal{W} = T(gh\eta_x)$ and $\mathcal{R} = h\mathcal{Q}_1(u)$. We recognize an elliptic operator in (2.2), to be solved for the non-hydrostatic term ϕ and where no time derivatives appear, and an hyperbolic part for system (2.3), in which the flow variables actually evolve. We notice that putting $\phi = 0$ allows us to recover the NLSW system. It is evident that this term models the effects of the non-hydrostatic pressure.

The decoupling of equation (1.25) into equations (2.2) and (2.3) is useful because it allows to apply, for each step, the most appropriate numerical method to discretize the space derivatives.

As a matter of fact, solving (2.2) using $(h^n, \mathbf{q}^n)$ implies the inversion of the matrix discretizing $(I+\alpha T)$ and it represents the most computationally demanding process of the entire algorithm. For this elliptic step, a classical C^0 Galerkin finite element method is used.
To this purpose, we consider a tesselation of the spatial domain composed by a set of non-overlapping elements. We denote by Δx the reference mesh size. In 1D, Δx can be defined as $\Delta x = x_{i+i} - x_i$[1]. Defining $\Theta = (\eta, \mathbf{u})$ at a certain time, this set of unknowns is interpolated in the nodes by means of the piecewise linear continuous shape function $\varphi_i(x)$ such as

$$\Theta_{\Delta x}(x,t) = \sum_i \varphi_i(x)\ \Theta_i(t) \tag{2.4}$$

The function $\varphi(x)$ is the well-known finite element basis function, which assumes value 1 in the node i and is null everywhere else. We have plotted φ in two dimensions in the left picture of Figure 2.1. In the right picture of Figure 2.1 we show the resulting interpolation for $\eta_{\Delta x}$. The same can be thought for all the quantities involved in the system: $h_{\Delta x}$, $b_{\Delta x}$, $\mathbf{u}_{\Delta x}$, $\phi_{\Delta x}$, interpolated in the nodes of the mesh.

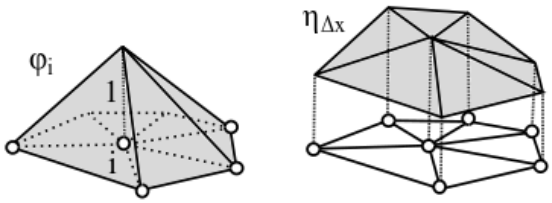

Figure 2.1 – Finite element: P^1 basis function (left) and interpolation (right)

Passing through the variational form of (2.2) and defining $\Phi = [\phi_1(t), \phi_2(t), ..., \phi_N(t)]^T$ and $\mathbf{U} = [\mathbf{u}_1(t), \mathbf{u}_2(t), ..., \mathbf{u}_N(t)]^T$ in the N nodes of the mesh, the discretized system is

$$\begin{aligned} (\mathrm{M}^G + \alpha \mathrm{T})\Phi &= \mathrm{W} - \mathrm{R} \\ \mathrm{W} &= \mathrm{T}\delta \\ \mathrm{R} &= \mathrm{Q}[h, \mathbf{U}] \end{aligned} \tag{2.5}$$

where T is the matrix deduced from (2.2) and Q is a non-linear operator; δ is an array containing nodal values of auxiliary variables introduced to handle the third order derivatives. The mass matrix M^G is symmetric, positive definite and constant. The matrix $(\mathrm{M}^G + \alpha \mathrm{T})$ is invertible thanks to the coercitivity property inherited from the continuous operators $(\mathbb{I} + \alpha \mathbb{T})$ ([Filippini et al., 2016]).

[1]The mesh is chosen uniform here for simplicity. For non-uniform meshes, the Δx is taken as the maximum value $\Delta x = \max(x_{i+i} - x_i)$ and the equations are slightly more complex.

Concerning the hyperbolic step, a finite volume scheme is a very suitable choice. The method currently implemented in the code at the CARDAMOM team is a node-centered scheme for which one evolves the averaged value over the median dual control cell C_i:

$$\bar{\Theta}_i(t) = \frac{1}{\Delta x} \int_{C_i} \Theta_i(x,t) \tag{2.6}$$

This allows to write equations (2.2) and (2.3) in a semi-discrete form as

$$\frac{\partial}{\partial t}\bar{\Theta}_i + \frac{1}{\mid C_i \mid} \int_{\partial\Omega} (\mathbf{F}\hat{n}^x + \mathbf{G}\hat{n}^y) = \frac{1}{\mid C_i \mid} \int_{\Omega} (\mathbf{S}_{b_i} + \mathbf{\Phi}) \tag{2.7}$$

with Ω the area of the cell C_i, $\partial\Omega$ its boundary and $\hat{n}$ the unit normal to that boundary (see Figure 2.2), along x and along y. $\mathbf{F}$ and $\mathbf{G}$ are the numerical fluxes at each cell interface in the x and y direction respectively and $\mathbf{S}_{b_i}$ is the topography source term. The term $\mathbf{\Phi}$ is the source stemming from the elliptic phase integrated over C_i.

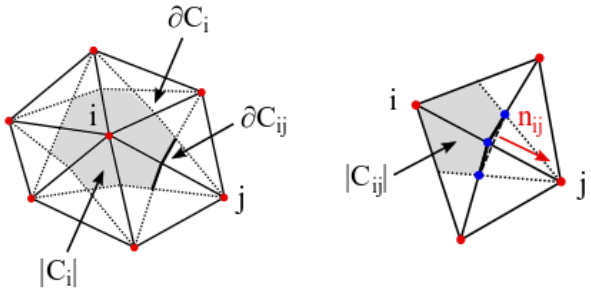

Figure 2.2 – Finite volume: median dual control cell definition for an internal node i of the mesh (left) and basic notation for the ij interface (right)

Because the non-hydrostatic part is the most expensive to solve, discretising the complete GN system requires a substantial amount of computational time. Running the NLSW model demands up to five times less than the GN model. Considering this great difference in computational cost, one can initially use the NLSW model as a first approximation, in order to have a quick idea of the solution, and then wait for the GN, more precise, solution.

Time Discretization

An explicit method is used in the time discretisation. The simpler is the explicit Euler method:

$$\begin{cases} (I + \alpha T)^n \phi^n = \mathcal{W}^n - \mathcal{R}^n \\ h^{n+1} = h^n - q_x^n \Delta t \\ q^{n+1} = q^n - (uq)_x^n \Delta t - (gh\eta_x)^n \Delta t + \phi^n \Delta t \end{cases} \tag{2.8}$$

where the superscript n indicates the variables at a certain time $t^n = n\Delta t$, if the time step chosen is Δt. As shown in system (2.8), the solution at time $t^{n+1} = (n+1)\Delta t$ is computed thanks to the solution obtained at the previous time. However, there are some higher-order methods that can give higher accuracy with respect

to the explicit Euler scheme, as the Runge-Kutta («RK») methods. In particular, the explicit Euler method is nothing but a RK1, i.e. a Runge-Kutta method of order 1. We can increase the order and approximate the solution with a RK2:

$$\begin{cases} (I+\alpha T)^n \phi^n = \mathcal{W}^n - \mathcal{R}^n \\ h^k = h^n - q_x^n \Delta t \\ q^k = q^n - (uq)_x^n \Delta t - (gh\eta_x)^n \Delta t + \phi^n \Delta t \end{cases} \tag{2.9}$$

$$\begin{cases} (I+\alpha T)^k \phi^k = \mathcal{W}^k - \mathcal{R}^k \\ h^{n+1} = \frac{1}{2}h^n + \frac{1}{2}h^k - q_x^k \frac{\Delta t}{2} \\ q^{n+1} = \frac{q^n+q^k}{2} - (uq)_x^k \frac{\Delta t}{2} - (gh\eta_x)^k \frac{\Delta t}{2} + \phi^k \frac{\Delta t}{2} \end{cases}$$

Higher orders can be derived similarly. The choice of the method is dictated by a compromise between accuracy and cost of application.
For the spatial discretization, high orders are used to minimise the error. It can be shown that the third order is necessary for the finite volumes in order to obtain an overall dispersion close to that of a fully 4^{th} order approximation ([Filippini, 2016]). Similarly, the time discretization must be of at least order 3; therefore, a RK3 scheme is used here.

We point out that the time step is actually defined as $\Delta t^{n+1} = t^{n+1} - t^n$ and it changes at every step, computed by means of the CFL condition:

$$\Delta t^{n+1} = \text{CFL} \frac{\Delta x}{\max_i(|u_i^n| + \sqrt{gh_i^n})} \tag{2.10}$$

Treatment of Wet/Dry Fronts

Water running-up the banks implies an issue for the numerical modelling: the definition of the limit between wet and dry areas. Normally, in an open channel, the center part is always submerged while on the banks there can be both wet and dry areas, changing with the travelling wave.
Deciding when a cell in the mesh must be considered dry is not trivial. In this case, we introduce two threshold parameters, ε_h^{wd} and ε_u^{wd}, acting indipendently on the water depth and velocity respectively. Basically, when the water depth gets values less than ε_h^{wd}, the corresponding cell is considered dry.
The velocity wet/dry parameter is necessary to avoid division by zero when computing u from $q = hu$. In particular, if in a node $h \leq \varepsilon_u^{wd}$, the velocity there is set to zero.

For a matter of absolute mass conservation, the total mass in the nodes that are considered dry is redistributed uniformly to the rest of the domain.

In our simulations, after some trials, it was found that the best choice for the parameters, in order to have a neat wave signal, is $\varepsilon_h^{wd} \sim 10^{-4}$ and $\varepsilon_u^{wd} \sim 10^{-7}$.

Modelisation of Wave Breaking

We have seen in section 1.4 that shoaling implies an increase in the wave amplitude when entering shallow water. In this situation, since the wave velocity depends on the water height, the top of the wave may travel faster than the toe. In reality,

the wave front steepens and steepens, becomes vertical and it is only a question of time before the wave crest overturns. The wave is thus broken and it dissipates energy in the turbulent flow originated.
The BT models provide a correct description of the waves up to the breaking point, but from this point on, they are no more correct. Some additional mechanism is therefore necessary. The NLSW equations, owing to their hyperbolic form, may have solutions developping shock discontinuities very early in the propagation. This feature can be however exploited to model breaking.

The algorithm implemented in the numerical model is delineated hereafter ([Kazolea et al., 2014]):

- Computation of wave breaking criteria for each computational cell.

  A wave is considered breaking when the vertical velocity component at the free surface exceeds a value proportional to the shallow water wave phase velocity, i.e. when $|\partial_t \eta| \geq \gamma\sqrt{gh}$, with the calibration constant $\gamma \in [0.3, 0.65]$, depending on the physical configuration. This *surface variation criterion* is not sufficient because it can be $\partial_t \eta \approx 0$ for stationary hydraulic jumps. It is thus combined with the *local slope angle criterion*: $\|\nabla\eta\|_2 \geq \tan(\phi_c)$, where ϕ_c is the critical front face angle at the initiation of breaking and its values are in the range $\phi_c \in [14°, 33°]$.
  In our simulations, we chose $\gamma = 0.6$ and $\phi_c \approx 30°$, as done in [Kazolea et al., 2014] too.

  The first criterion is easily calculated during the running of the model, the second acts complementary to the first one and corrects its limitation.

- Each mesh node is checked and if at least one of the criteria is satisfied, the relative node is flagged as breaking.

- Different breaking waves are distinguished by creating a dynamical list that contains the breaking nodes of each wave.

- Each breaking wave is treated individually.

  Here we switch from GN equations to NLSW, locally in time and space, by setting $\phi = 0$ in equations (2.2) and (2.3). Only the hyperbolic part is solved for the wave fronts and the breaking wave dissipation is represented by shock energy dissipation. This strategy is kept until bores stop breaking, i.e. when their Froude number drops below the critical value $Fr_c \approx 1.3$ (see below).

- If $Fr < Fr_c$, a switch is done back to BT model for non-breaking undular bores.

  This criterion is based on the computation of the local Froude number whose definition

$$Fr = \sqrt{\frac{(2H_2/H_1 + 1)^2 - 1}{8}} \tag{2.11}$$

  is derived from the analogy between a broken wave and a bore in the sense of a simple transition between two uniform levels. Since every wave is treated individually, H_1 and H_2, defined as in Figure 2.3, can be easily found by computing the minimum and the maximum water depth respectively among

all the breaking nodes corresponding to a certain wave.
If the condition $Fr < Fr_c$ is satisfied, all the breaking points of the wave are unflagged and the wave is considered non-breaking.

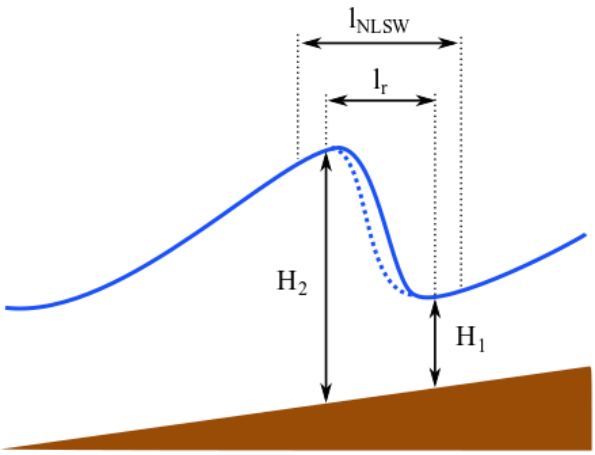

Figure 2.3 – Sketch of a roller wave and definition of the breaking zone

- For each breaking wave, extension of the computational region governed by the NLSW equations.

  Along the wave direction there is a region, roughly centered around the wave front, where the NLSW equations are applied; it is limited by the quantity $l_{NLSW} = [x_{min}, x_{max}] \times [y_{min}, y_{max}]$ (Figure 2.3), using the breaking node's minimum and maximum x-coordinate and y-coordinate.

  Outside this zone, the BT equations are applied. At the interface, some non-physical effects may appear due to the relatively strong variations that may exist in the solution, which affect the estimation of the dispersive terms.
  In order to obtain a smoother link between the two different models, the NLSW region is enlarged: $l_{NLSW} = [x_{min} - \delta_x, x_{max} + \delta_x] \times [y_{min} - \delta_y, y_{max} + \delta_y]$, where $\delta_x = \max(2.5\ l_r - (x_{max} - x_{min}, 0)$ and $\delta_y = \max(2.5\ l_r - (y_{max} - y_{min}, 0)$, being $l_r \approx 2.9(h_2 - h_1)$ the physical length of the wave roller[2].

[2]The surface roller is an aerated white water region which rides the underlying breaking wave, is stationary relatively to the wave crest and therefore moves with the wave speed.
From Svendsen, I.A., Wave heights and set-up in a surf zone, *Coastal Engineering*, 8(4):303-329, 1984.

Chapter 3

Test Cases

Open channels can have various bed shapes but looking at what nature and men do, two main geometrical approximations can be done: a rectangular and a trapezoidal configuration. Previous works on bore propagation in this type of channels provide experimental and numerical data that are used in this work to validate the latest version of the code.

3.1 Undular Bore in a Rectangular Channel

The most simple bed shape is certainly the rectangular one, with flat bottom; it is also the first configuration to be studied in the past.

3.1.1 Experimental Data and Theoretical Models

Indeed, the first experiments on rectangular channels are performed by [Favre, 1935]: being the first one to observe the undular motion creating at the bore front, these secondary waves are named after him. [Treske, 1994] carried out some experiments on a rectangular channel too, together with measurements in a trapezoidal channel. These two experimental campaigns give us the references for the validation of the numerical methods presented here.

To complement field measurements in the validation, we also consider the theory by Lemoine for secondary waves ([Lemoine, 1948]). We will outline the basic ideas hereafter.
First of all, Lemoine assumed that the Rankine-Hugoniot relations, true for a breaking bore, are valid for an undular bore as well. He considered that the secondary waves propagate at the same speed than the bore: the undulations are therefore stationary in the referential of the bore and only one wavelength verifies the equality $c_\phi + u_2 = c_b$, so dispersion is not taken into account. Concerning the energy, his assumptions are in accordance with what explained in section 1.5: for high Froude numbers, energy is dissipated by turbulence, but for low Froude numbers the same energy is distributed among the secondary waves.
This theory derives from a sinusoidal model for waves of small amplitude and it gives the variation of the wavelength and the wave amplitude with the Froude number. This is obtained by using the dependence of c_ϕ on the wave number, and inverting the dispersion relation. Briefly speaking, it can be summarised as:

$$\begin{cases} c_b - u_2 = f(Fr) \\ c_\phi = \frac{\omega(k)}{k} \end{cases} \quad \rightarrow \quad \lambda \frac{\omega(2\pi/\lambda)}{2\pi} = f(Fr) \tag{3.1}$$

from which the expression of $\lambda = f(Fr)$ can be derived. From the wave steepness relationship ([Bonneton et al., 2015])

$$\frac{A}{\lambda} = \frac{4}{3\sqrt{2}\pi}(Fr-1)^{3/2} \tag{3.2}$$

the expression of $A = f(Fr)$ is obtained.

Despite all the hypothesis, Lemoine's theory represents well the reality. Therefore, having in mind all the restrictions of the case, we can use it as a guide for the validation of the numerical methods.

In particular, what we are interested in is, as Lemoine, the evolution of two main parameters of the wave: the wavelength and the amplitude. In Figure 3.1 we have sketched the values experimentally measured: the characteristics of the first waves of the undular train. The choice is probably due to the fact that these parameters change along the wave train, as pointed out by [Lemoine, 1948].

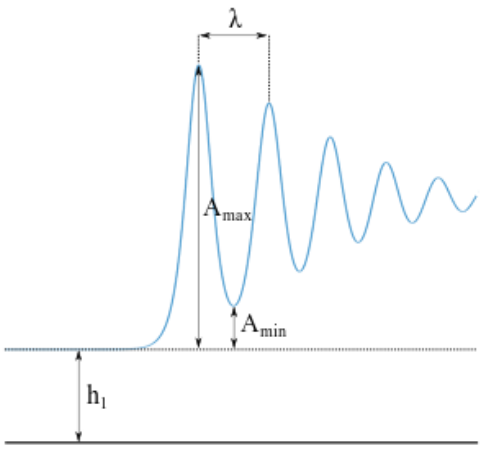

Figure 3.1 – Measurement of wavelength and amplitudes of the undular bore

3.1.2 Numerical Simulations

We start by reproducing the experiments led by Treske. We consider an open rectangular channel of width $w = 1{,}24\,\text{m}$, with initial upstream conditions $h_1 = 0{,}16\,\text{m}$ and $u_1 = 0\,\text{m/s}$. The actual computational domain is half the channel (i.e. of width $w/2$), but the complete solution can be found exploiting the symmetric condition with respect to the longitudinal direction. Simulations are carried out for both NLSW and GN models for a range of Froude numbers of $Fr = [1.05, 1.30]$.

The channel is 40 m[1] long and the free surface signals are taken at time $t = 23\,\text{s}$, close to the final time. The spatial resolution is chosen as $\Delta x = 0{,}02\,\text{m}$ and $\Delta y = 0{,}05\,\text{m}$. This choice is derived by the need to have enough nodes along a single wave in order to model it properly. Bigger space intervals would lead to an unacceptable approximation for the shortest waves and, as it is easily seen, the requirement is stricter in the propagation direction.
The NLSW model, because of its lack of dispersive terms, does not predict the undular motion (as already seen in section 1.3.3, for the one-dimensional case) and it transforms the initial change in water depth into an abrupt discontinuity, as shown in Figure 3.2. For all Froude numbers, the wave steepens when travelling into the channel and it eventually breaks. The ability of the NLSW model in creating a breaking bore is confirmed both for high Froude numbers, which is consistent with field observations, and for low Froude numbers, for which no wave breaking is observed in reality.

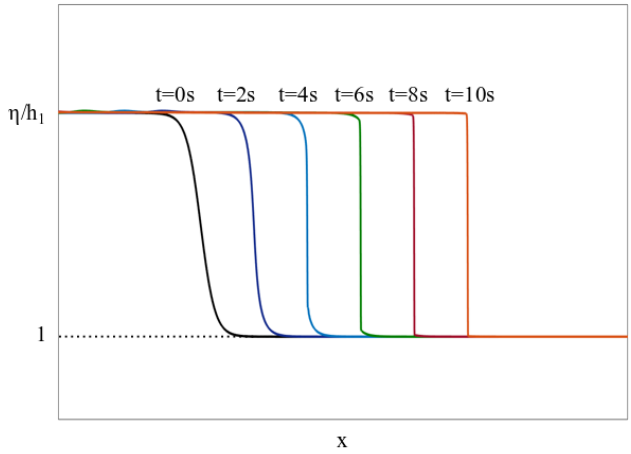

Figure 3.2 – Time evolution of the free water surface in a rectangular channel

The GN model, instead, develops the secondary waves during the propagation of the bore; this train has a distinctive shape (Figure 3.3): from a maximum amplitude at the front of the bore, the oscillations exponentially decrease and dissolve around the new water depth h_2.

[1]The channel must be taken long enough to allow the undular motion to stabilize and develop at least 2 or 3 crests. The variation of λ with the channel length has been analysed, for $L = 25\,\text{m}$, $L = 50\,\text{m}$ and $L = 100\,\text{m}$, giving some - negligible - percentage of discrepancy among the results. Taking into account the stationarity of the solution and the computational costs, a good compromise has been chosen and thus $L = 40\,\text{m}$.

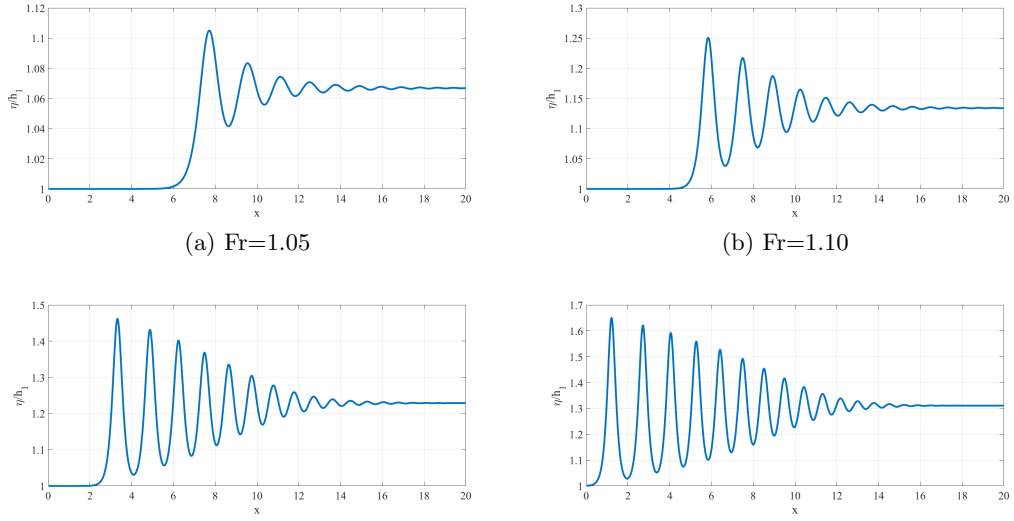

(a) Fr=1.05 (b) Fr=1.10

(c) Fr=1.17 (d) Fr=1.23

Figure 3.3 – Solution at $t = 23\,\mathrm{s}$ of the undular bore in a rectangular channel, for different Froude numbers

To have an idea on how the bore is travelling in reality, we refer to Figure 3.4 for a 3D representation of the solution.

For high Froude numbers, thanks to the breaking model discussed in chapter 2, the bore breaks and almost no wave train is generated behind it. The amplitudes of the secondary waves are modest and the shape of an hydraulic jump can be distinguished.

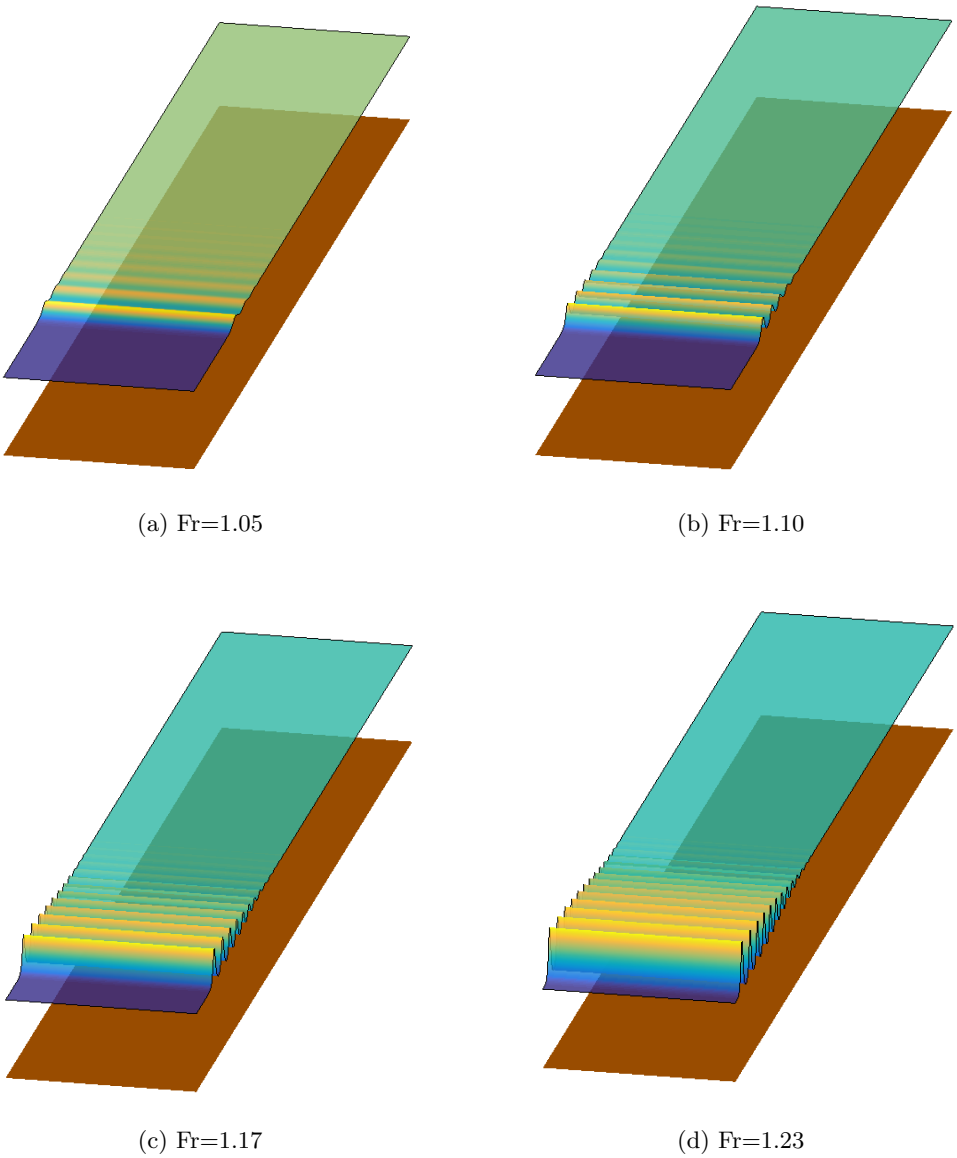

(a) Fr=1.05

(b) Fr=1.10

(c) Fr=1.17

(d) Fr=1.23

Figure 3.4 – 3D visualisation of the solution at $t = 23\,\mathrm{s}$ of the undular bore in a rectangular channel, for different Froude numbers

From a more quantitive point of view, the wavelength shows an evolution with the Froude number (Figure 3.5): for low Froude numbers, λ is quite big and it reduces with the increasing strength of the bore until breaking, where no wavelength can be detected.

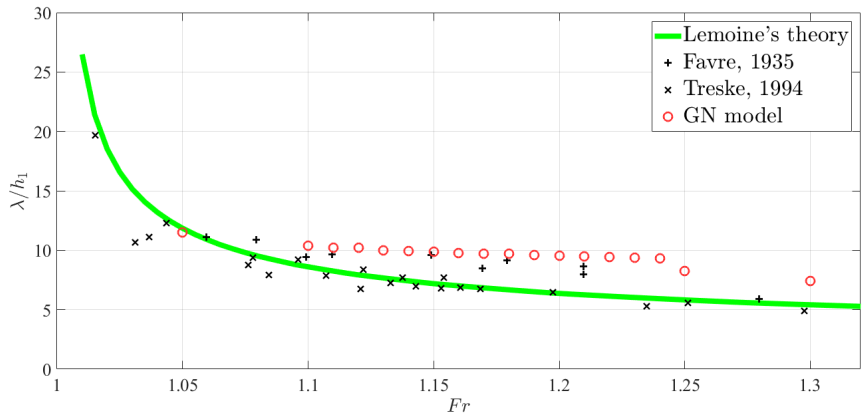

Figure 3.5 – Evolution of the bore wavelength with the Froude number in a rectangular channel

Figure 3.5 shows also the Lemoine's theory curve: although the wavelength resulting from the simulations is slightly higher, it represents well the evolution with the Froude number. In particular, Lemoine's theory is appropriate for Treske's data and our results find a closer correspondence with Favre's data. For very low Froude numbers, Lemoine's theory predicts very long waves, which are rarely seen in Treske's experiments and in our simulations.

Concerning the amplitudes (Figure 3.6), we can see that the gap between A_{max} and A_{min} first increases as the Froude number increases and then reduces when reaching breaking, in accordance with the visual interpretation (Figure 3.3).

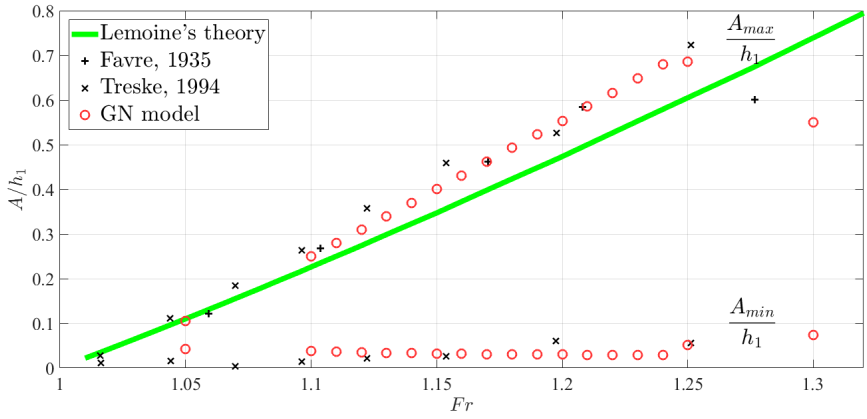

Figure 3.6 – Evolution of the bore amplitudes with the Froude number in a rectangular channel

Lemoine's theory shows a good prediction for A; it is however erroneus for the amplitude at high Froude numbers: it can't predict breaking so it gives a continuous, unreal growth.
Our numerical results are in good accordance with the ones from [Chassagne, 2017] too, sometimes even closer to Lemoine's theory and experimental data.

3.2 Undular Bore in a Trapezoidal Channel

Admitting only rectangular shapes for natural and artificial channels is too restrictive: it's hard to find channels of perfect shape and normally banks are sloped. Trapezoidal sections are a good compromise between reality and simplicity of modelling.

3.2.1 Experimental Data and Theoretical Models

In this spirit, [Treske, 1994] carried out experiments on trapezoidal channels, reporting a transition in the flow behaviour for relatively low Froude numbers. More recent field measurements by [Bonneton et al., 2015] in real estuaries are in good agreements with Treske.

If we recall the flow in the rectangular channel, we can consider the flow field one-dimensional and identify a transition from an undular bore to a turbulent bore, approximatively around $Fr = 1.30$; for the trapezoidal case, Treske noticed two transitions: the one already mentioned and a new one, for $Fr \sim 1.15$. For the latter transition, we define the transition Froude as Fr_{t_1}. We use Fr_{t_2} for the transition to turbulent flow.

Qualitatively, around Fr_{t_1}, the bore front is not uniform any more (Figure 3.7), there is probably some interactions of the waves with the sloping banks; from the top view, it looks like a cross is forming on the waves crests. For high Froude numbers, the dynamics is even more evident (Figure 3.8). The flow at the banks is therefore quite different from the flow in the center of the channel: this diversification oblige us to consider the flow field bi-dimensional.

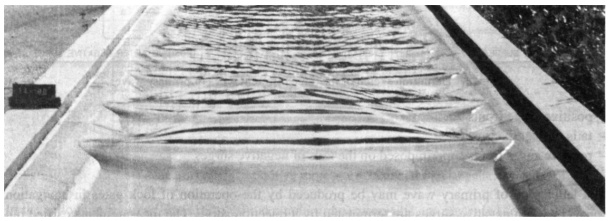

Figure 3.7 – Undular bore at $Fr = 1.12$ in a trapezoidal channel - Experimental results by [Treske, 1994]

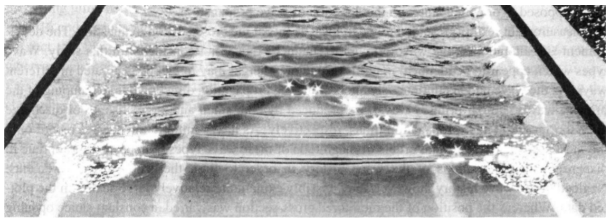

Figure 3.8 – Undular bore at $Fr = 1.24$ in a trapezoidal channel - Experimental results by [Treske, 1994]

Lemoine's theory cannot be used to model the waves appearing before Fr_{t_1}. A *ad hoc* linearized theory can however be written for the trapezoidal channel ([Chassagne, 2017]).
The theory is based on the linearized Saint-Venant equations for the unknowns

η, u, v, where the free surface function is represented as the mean value in the transversal direction, y. We define the parameter $\vartheta = L_y/L_x$, where L_y is the transversal channel length and L_x is the longitudinal length in the direction of the wave propagation. Assuming ϑ to be small, we can express the three unknowns as an asymptotic development of ϑ. The smallness hypothesis for ϑ corresponds to the assumption that the propagation of perturbations in the flow direction takes place on a larger scale than that of the transversal variation of the bathymetry. Another adimensional parameter is introduced, ϵ, as the ratio of the amplitude of the perturbation to the water depth at rest; ϵ represents the degree of non-linearity and it is assumed to be $\epsilon \ll 1$, $\epsilon \ll \vartheta$. In this case, all the non-linear terms in the equations can be neglected: we obtain a linearized theory, from which a dispersion relation can be deduced. It results that the phase velocity is not constant with the wavenumber and thus dispersion is present. Following the same approach than Lemoine, the evolution of the wavelength and the amplitude can be found as functions of the Froude number. For more details, the reader can refer to [Chassagne, 2017].

In this case too, the theory needs some hypothesis, sometimes some strong ones. Keeping that in mind, it is still very useful as a first prediction of the numerical results.

3.2.2 Numerical Simulations

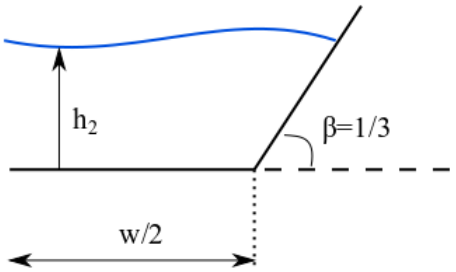

Figure 3.9 – Sketch of the geometry of a trapezoidal channel. The banks slope is fixed at $\beta = 1/3$.

Figure 3.9 represents the setting of the problem: the geometrical parameter are the same as for the rectangular channel, except for the introducion of a new one: β, the inclination of the banks with respect to the horizontal. A remark must be done on this variable: it is not an angle but a non-dimensional parameter standing for the tangent of the banks inclination angle. Thus when we speak of $\beta = 1/3$, we mean an angle of the banks of about 18°.

The initial solution is still computed from the Rankine-Hugoniot relations but, since the geometry is slightly more complex, the equations are also more complicated. Moreover, the initial solution is the same as (1.34), with the hyperbolic tangent function, but now for h we have to take into account the bathymetry too, which is a function of y.

Therefore, we have

$$
\begin{aligned}
h(x, t=0) &= \frac{h_2 - h_1}{2} \tanh\left(\frac{x - x_0}{l_t}\right) + h_2 - b(y) \\
u(x, t=0) &= \frac{u_2 - u_1}{2} \tanh\left(\frac{x - x_0}{l_t}\right) + u_2 \\
v(x, t=0) &= 0
\end{aligned}
\tag{3.3}
$$

The initial velocity expression doesn't change and it is assumed to be the same both in the axis and at the banks.

As done before, we impose some geometrical and flow parameters, inspired by Treske's experiments: $w = 1{,}24\,\mathrm{m}$, $\beta = 1/3$, $h_1 = 0{,}16\,\mathrm{m}$, $u_1 = 0\,\mathrm{m/s}$ and $Fr = [1.05, 1.30]$. Once again the computational domain is reduced to half channel, as shown in Figure 3.9 and the entire solution is recovered by symmetry.

We could expect the NLSW model to give, as for the rectangular channel, the propagation of a breaking bore at all Froude number. However, we can see in Figure 3.10(a) the presence of secondary waves.

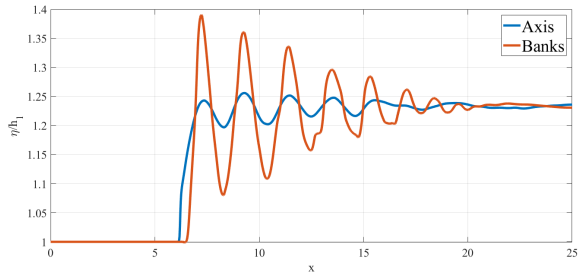

(a)

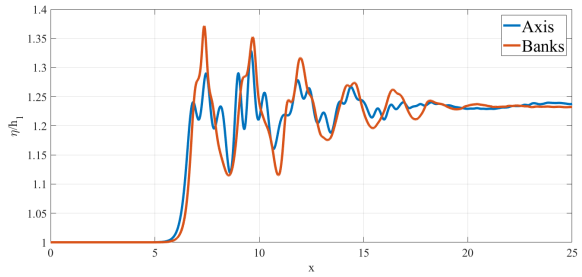

(b)

Figure 3.10 – Free surface elevation along the axis and along the banks of a trapezoidal channel ($\beta = 1/3$) at $Fr = 1.20$ for (a) SW model and (b) GN model

The NLSW equations don't contain dispersive terms, but the transverse variation of the bathymery induces diffraction and refraction of the waves such that we get some dispersive-like effects. The physics predicted by the NLSW model is still different from reality: as a matter of fact, we can't see the change of dynamics between axis and banks that appears in real life and when using the GN model (Figure 3.10(b)). The latter, containing the NLSW one, is able to combine refraction with dispersion and the result is in good accordance with Treske's results.

In Figure 3.11 we can see a 3D representation of the GN solution before and after transition: the two regimes are comparable to Treske's data (Figures 3.7 and 3.8).

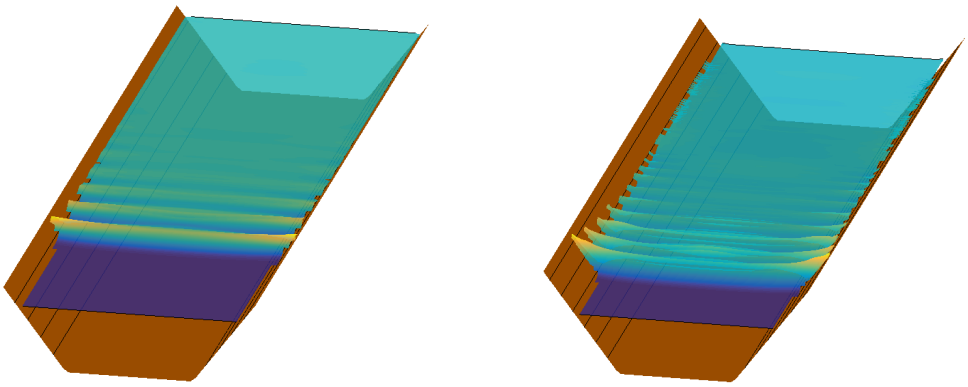

(a) Fr=1.10 (b) Fr=1.24

Figure 3.11 – 3D visualisation of the solution of the undular bore in a trapezoidal channel ($\beta = 1/3$), for (a) $Fr = 1.10$ and (b) $Fr = 1.24$, i.e. before and after transition.

The comparison is possible also quantitatively, as seen in Figure 3.12.

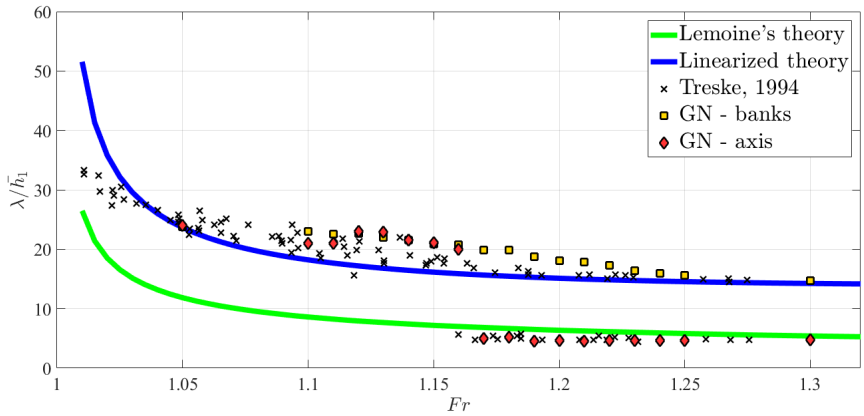

Figure 3.12 – Evolution of the bore wavelength with the Froude number along the axis and the banks of a trapezoidal channel with $\beta = 1/3$

Along the banks, we have an evolution of the wavelength similar to the one in the rectangular case, but shifted to lower frequencies.
Along the axis, we can see the transition, here for $Fr_{t_1} = 1.16$, from the trapezoidal banks condition back to the rectangular wavelengths: higher frequencies have appeared and they are kept until high Froude numbers. At $Fr = Fr_{t_2}$ we have the second transition, common to all channel shapes, due to wave breaking.

We may say that the NLSW model, the linearized theory - which is derived from NLSW equations - and the GN model are in good accordance until the transition at Fr_{t_1}. The GN model bifurcates at this point and the wavelengths along the axis fall on the Lemoine's theory line.

Figures 3.13 and 3.14 show that the amplitude evolution is the same for axis and banks and for the rectangular channel, but here the values are different with respect to which part of the channel section is chosen: amplitudes along the banks are wider than along the axis, as explained in section 1.4. Moreover, there is a jump in the amplitudes along the axis (Figure 3.14) after the transition because of the post-processing strategy.

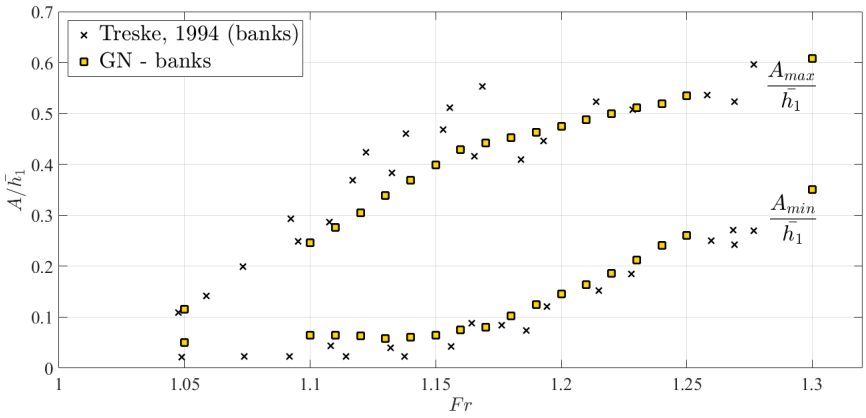

Figure 3.13 – Evolution of the bore amplitudes with the Froude number along the banks of a trapezoidal channel with $\beta = 1/3$

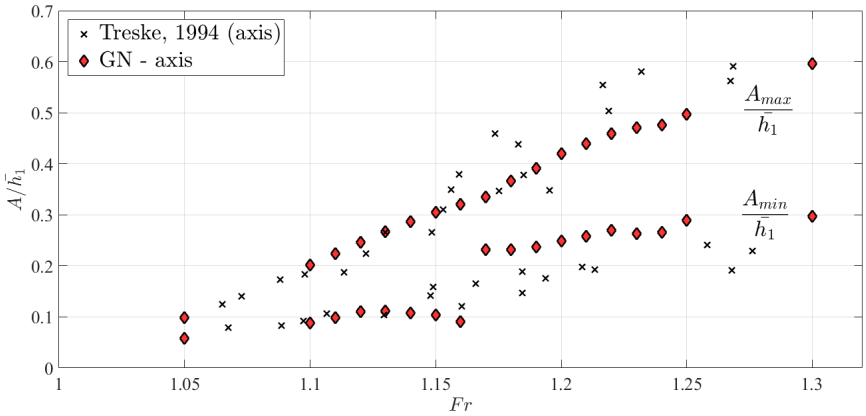

Figure 3.14 – Evolution of the bore amplitudes with the Froude number along the axis of a trapezoidal channel with $\beta = 1/3$

Chapter 4

Applications

The work of [Chassagne, 2017] discussed in the previous chapter is part of the various numerical analysis on the dynamics in open channels carried out hitherto. It shows the capabilities of the GN models to reproduce these dynamics, and proposes a linear theory for the hydrostatic low Froude number dispersive-like mode. These results encourage to push the study further.
From the simple rectangular and trapezoidal channel shapes, one can think of enlarging the range of possibilities to irregular, non-symmetric, bed-changing channels or taking into account sediment transportation, viscosity, natural and articial obstacles and many other inputs that would give a description of the problem closer to reality.

In this work we investigate the dependence of the transition Froude number Fr_{t_1} on the slope of the banks.

4.1 Undular Bore in a Channel with Sloping Banks

The geometry of the channel is characterised by the width w, and by the banks inclination β. The flow regime is determined by the Froude number. Just as done in the aeronautical field for airfoils, we want to keep the study general and suitable for any scale: to do so, we must consider non-dimensional parameters. Fr and β don't have any dimension by definition, but the width is thus redefined as w/h_1.

In order to analyse one effect at the time, we decide to keep w/h_1 constant and we study the dynamics when the other two parameters vary.
So if we suppose a symmetric bed and $\beta \neq \{0, \infty\}$, the starting point is still a trapezoidal channel, but unlike the one of section 3.2, now the banks can vary their inclination (Figure 4.1).

The assumption of symmetry allows once again to limit the computational domain to half the channel, in the longitudinal sense, and the solution is then mirrored for visual analysis.

4.1.1 Setting of the Problem

As displayed in Figure 4.1, we analyse banks with β in the range $[1/6, 4]$. In general, tidal bores occur in fluvial estuaries, for which the banks slope is in the range 0.1-0.3 ([Bonneton et al., 2015]). Thus $\beta = 1/6$, or either about 10° of inclination, is an appropriate choice of minimum slope. The choice of this minimum β is corroborated by the fact that for smaller slopes, the water distributes more along

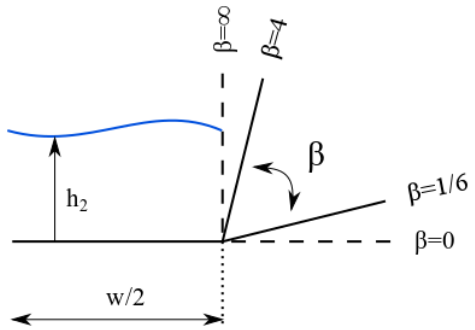

Figure 4.1 – Half trapezoidal channel with variable banks inclination

the banks, thus moving the wet/dry line further and forcing to widen the computational domain. This phenomenon is not easy to predict and the computational cost would be increased. The upper boundary $\beta = 4$, or an angle of about 76°, is a dozen degrees from the limit case of vertical banks. Such an important banks inclination is considered in order to study the wave dynamics in manmade rivers.

The Froude number is still in the range $[1.05, 1.30]$ and the initial solution is the same as for the previous simulations: $h_1 = 0{,}16\,\text{m}$, $u_1 = 0\,\text{m/s}$; $w = 1{,}24\,\text{m}$ just as in Treske's experience. Treske didn't explore the case with sloping banks and we don't have any data about it from anyone else, neither empirical nor numerical. Therefore, we compare our results with Lemoine's theory and the linearized theory by [Chassagne, 2017].

More than a dozen different inclinations of the banks are analysed in the range decided for β using the same basic structured grid (Figure 4.2), the same one used in sections 3.1 and 3.2. We recall that $\Delta x = 0.02$ and $\Delta y = 0.05$.

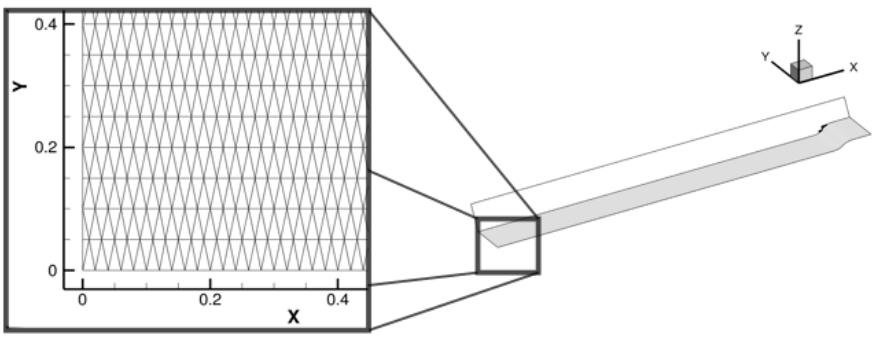

Figure 4.2 – Zoom of the mesh grid

Actually, since β changes, the extension of the mesh changes as well, as displayed in Figure 4.3.

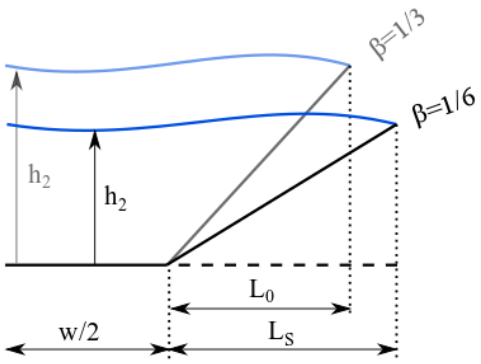

Figure 4.3 – Variation of the geometry with $\beta < 1/3$

Instead of changing the mesh for every angle to keep Δy constant, we stretch and contract the basic grid thanks to a scaling factor based on L_S, the horizontal projection of the new bank, being L_0 the projection of the basic bank, i.e. for $\beta = 1/3$. In this way, Δy changes with every different mesh but not excessively, so this variation can be accepted. Some tests were conducted in order to verify the assumption.

Post-processing

One of the major difficulties is to post-process the numerical solutions. To get the wavelengths and the amplitudes, one must recognize the transition; sections of the 2D time dependent data have been extracted to this end. The phenomenon of the transition is not abrupt and, in some cases, requires a non trivial choice for Fr_{t_1}. We can see the evolution for $\beta = 1/6$ with the Froude number in Figure 4.4. A first issue is discriminating real crests and signal noise (see for example Figure 4.4(b),(i) - the banks line). Then an uncertainties arise when discerning the creation of high frequencies over the basic signal (especially Figure 4.4(d),(e),(f), for the axis). For this second issue, some "objective" methods have been considered in a first time, such as using wavelets on the space signal in order to detect the creation of the high frequencies, but as results weren't conclusive, we have discarded this solution.

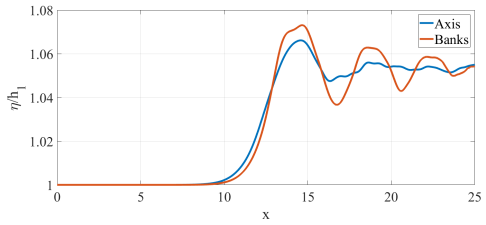

(a) Fr=1.05

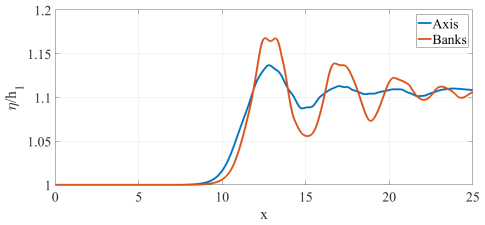

(b) Fr=1.10

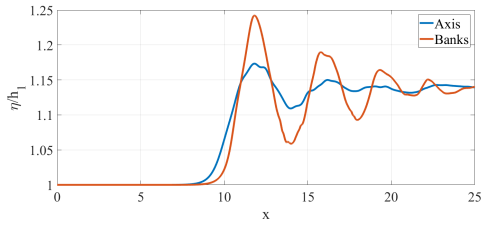

(c) Fr=1.13

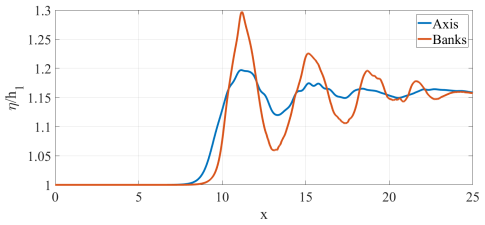

(d) Fr=1.15

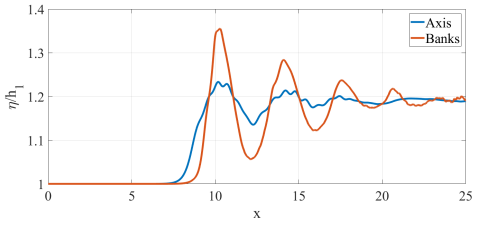

(e) Fr=1.18

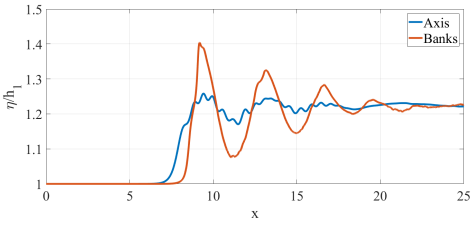

(f) Fr=1.21

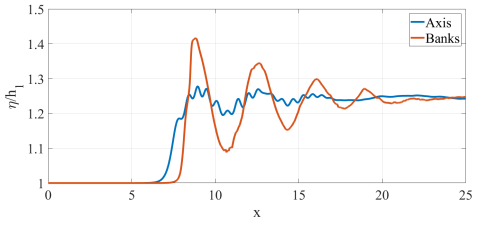

(g) Fr=1.23

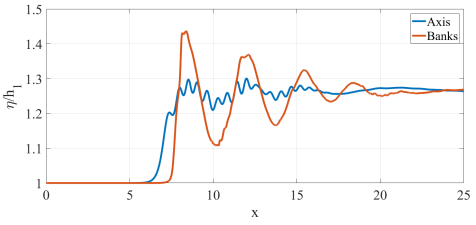

(h) Fr=1.25

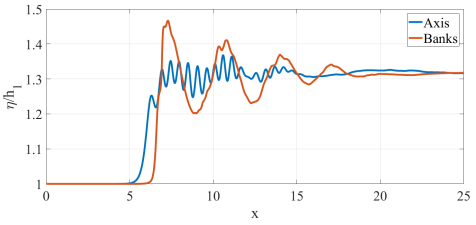

(i) Fr=1.30

Figure 4.4 – Evolution of the space signal with the Froude number, for $\beta = 1/6$

Concerning the difficulty in discerning the wavelength, an analysis on the experimental and numerical methods used for the computation of λ was carried out in a first time. In particular Treske, during his experiments ([Treske, 1994]), measured the water level curvature by mean of three gauges installed across the main cross-section of the channel. The information recorded by the gauges was thus a signal in time from which he could get the wave period T. The wavelength was then obtained with the relation $\lambda = c_b T$, using the propagation speed calculated with the jump conditions. In our case, we can put some fictional gauges and replicate the same procedure as Treske; however, we can also obtain the signal in space at a particular time and directly determine the wavelength. This is what is done in [Chassagne, 2017] too, in which the wavelength is computed as the distance between two wave peaks.
The main feature of both methods is the quality of the signal: in the rectangular channel, the undular wave is neat and the peaks are easily detectable. When passing to the trapezoidal channel, the signal is slightly noisier but one can still distinguish the wave crests.

For many values of β, the flow interacts in different ways with the banks and it produces a more complex dynamics (Figure 4.4(b)). For this reason, we introduced a different method for the computation of the wavelength, as shown in Figure 4.5. The definition of λ doesn't change but instead of being computed between two peaks, is it computed between two mean values of points taken at the same height.

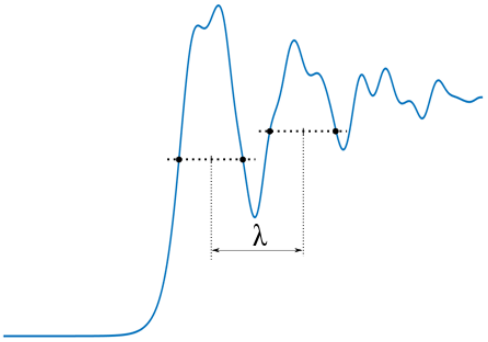

Figure 4.5 – Post-processing strategy to individuate the wavelength

This solution creates a new issue: the homogenisation of the results. Indeed, the peaks are normally not simmetric but slightly leaning forward or backward and this shape is not considered if the values are taken quite distant from the peak (as in Figure 4.5). The analysis of the wavelength is thus affected. However, estimating the error committed using this technique is not straightforward. If we compare the wavelengths using this mean-value techinque with the peak-value technique, we obtain a relative difference that can go from some percentage to almost 20%. A trend with Fr or with β is not discernible. Since the peak-value method is proved to be too tricky, especially close to the transition, we decided to compute the wavelength as in Figure 4.5, keeping in mind the drawbacks of this technique.

In addition, the flow signal, such as those represented in Figure 4.4, depends on where it is taken along the channel. If locating the axis is pretty easy, deciding where to take the signal on the banks is not trivial at all. Some discrepancies in our results could be caused by this choice, especially in the amplitudes. However, we are more interested in the evolution of the wavelength, which is not relevantly affected by the position along the banks. In any case, for consistency, we take the signal every time at the same place. This position is chosen taking into account that the wet/dry front varies not only with time but also with the various β.

The post-processing remains thus strictly linked to personal discretion; however, if it is carried out in the same way all the study long, conclusions don't lose their validity.

4.1.2 Results

For the different banks inclinations, the trend of the wavelength doesn't change: while the banks see a light reduction of λ with Fr, the axis witnesses an abrupt change of values in correspondance of a certain Froude number. We can see the results for the well-known case $\beta = 1/3$ in Figure 4.6.

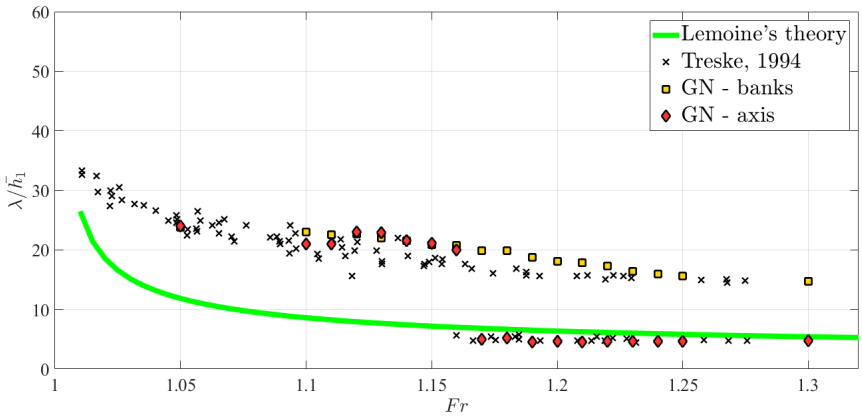

Figure 4.6 – Evolution of the bore amplitudes with the Froude number of a trapezoidal channel with $\beta = 1/3$

If we move to lower values of β, as $\beta = 1/6$ (Figure 4.7) and $\beta = 1/4$ (Figure 4.8), we first notice that the dynamics is the same but the Fr_{t_1} is different than that of the case $\beta = 1/3$.

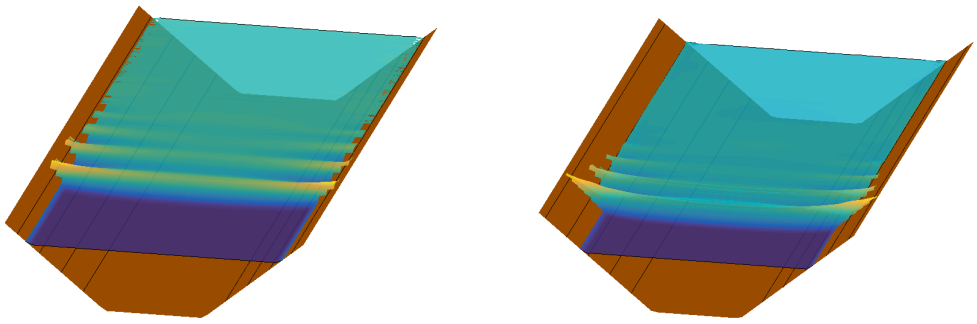

(a) Fr=1.13 (b) Fr=1.25

Figure 4.7 – 3D visualisation of the solution of the undular bore in the trapezoidal channel with $\beta = 1/6$ before and after transition.

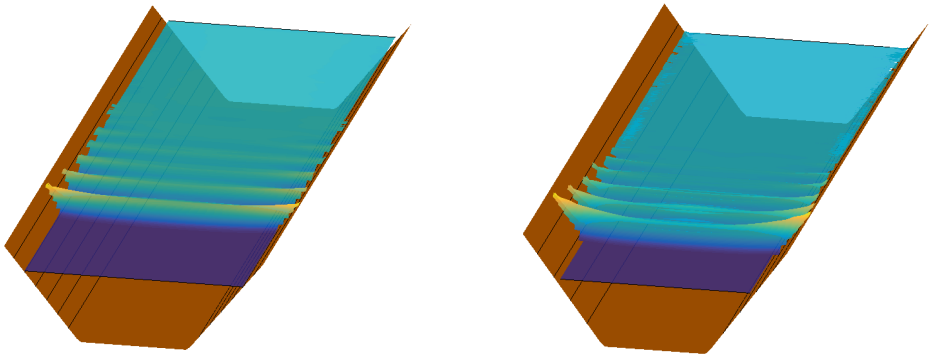

(a) Fr=1.12 (b) Fr=1.21

Figure 4.8 – 3D visualisation of the solution of the undular bore in the trapezoidal channel with $\beta = 1/4$ before and after transition.

In particular, transition takes place later for lower β (Figures 4.9 and 4.10). Moreover, the jump in the values is higher because waves before the transition are longer.

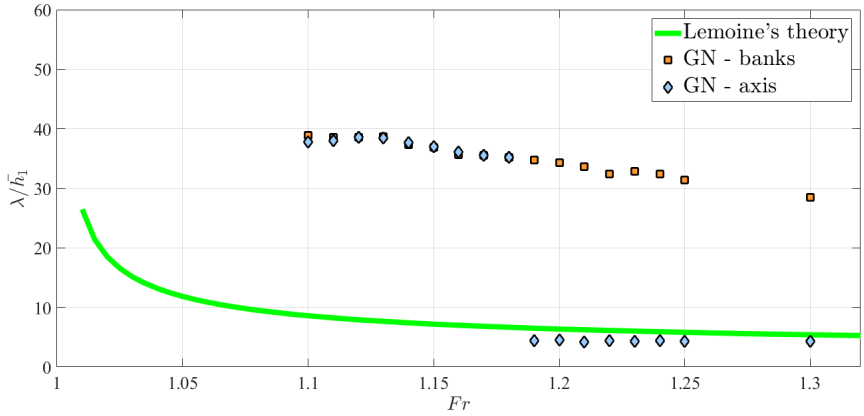

Figure 4.9 – Evolution of the wavelength with Fr for a trapezoidal channel with $\beta = 1/6$

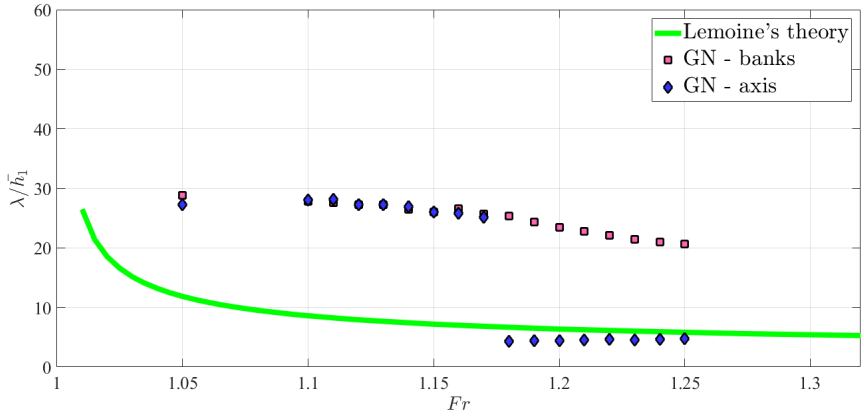

Figure 4.10 – Evolution of the wavelength with Fr for a trapezoidal channel with $\beta = 1/4$

For $\beta > 1/3$, a similar but opposite trend is obtained, with lower values for λ and with a lower Fr_{t_1}. Figures 4.11 and 4.12 show the results for the case $\beta = 1/2$.

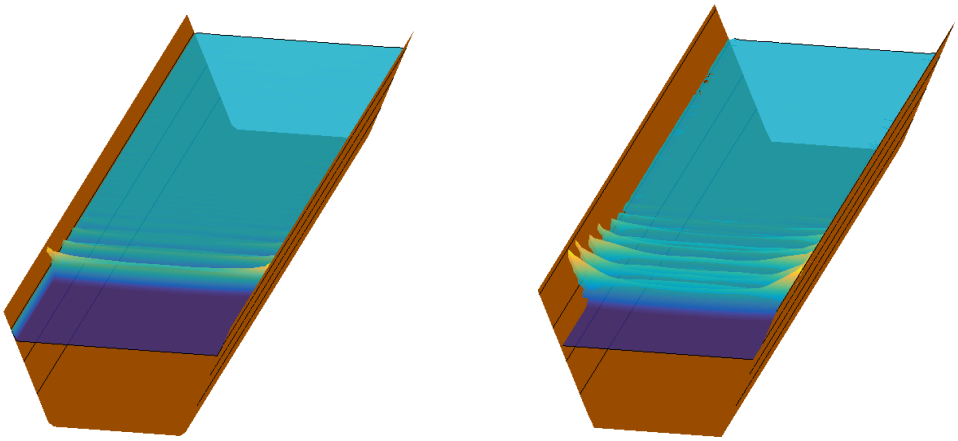

(a) Fr=1.10 (b) Fr=1.20

Figure 4.11 – 3D visualisation of the solution of the undular bore in the trapezoidal channel with $\beta = 1/2$ before and after transition.

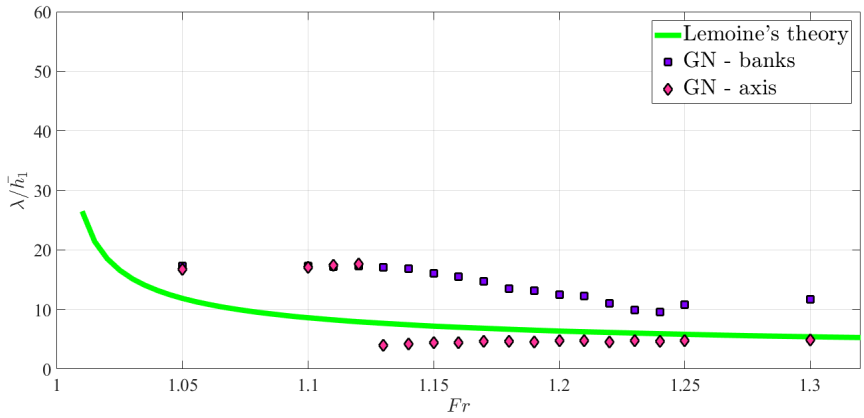

Figure 4.12 – Evolution of the wavelength with Fr for a trapezoidal channel with $\beta = 1/2$

There is a progressive translation to small λ when the banks are less and less sloping, i.e. when the trapezoidal channel gets closer to the rectangular one. We can see, for example, the case $\beta = 2/3$ (Figures 4.13 and 4.14), for which the results are lower than those shown before.

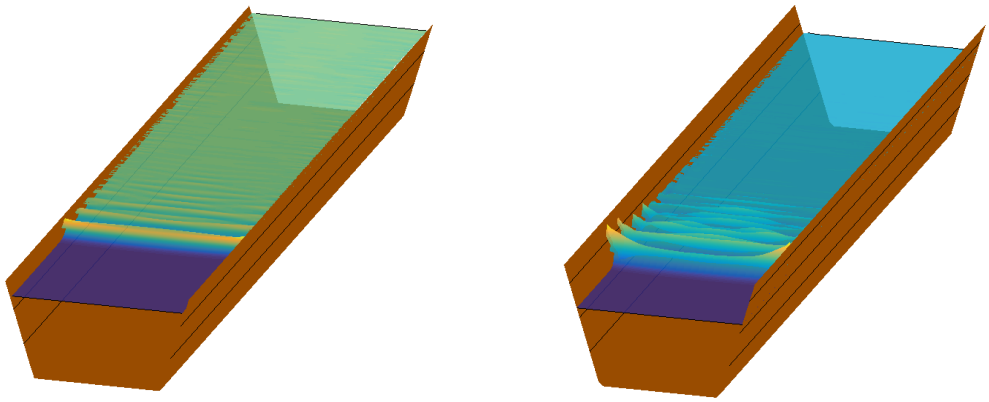

(a) Fr=1.07 (b) Fr=1.15

Figure 4.13 – 3D visualisation of the solution of the undular bore in the trapezoidal channel with $\beta = 2/3$ before and after transition.

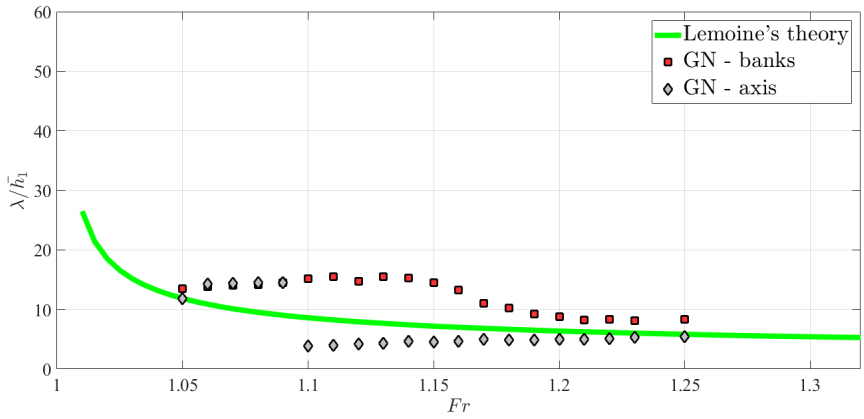

Figure 4.14 – Evolution of the wavelength with Fr for a trapezoidal channel with $\beta = 2/3$

For angles of about 40° and more, no transition can be detected and the behaviour is similar to the rectangular channel, except for the values of the wavelengths. Surely we can see from Figure 4.15 that the evolution is quite continuous and there isn't a Fr_{t_1}. The results follow the Lemoine's theory evolution but the values are slightly higher. For higher β, results would eventually fall on the theoretical line and the channel would be considered rectangular.

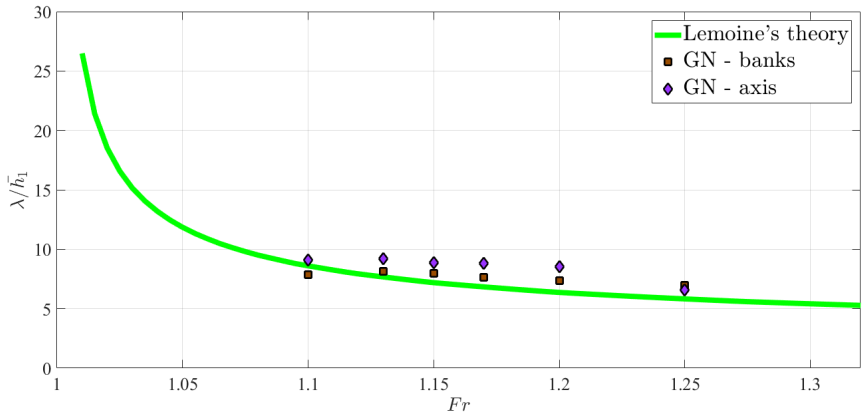

Figure 4.15 – Evolution of the wavelenth with Fr for a trapezoidal channel with $\beta = 4$

Similar trends are exhibited by the other β analysed but the results shown here are limited to few significant cases.

The dynamics observed can be summarised as in Figures 4.16, 4.18 and 4.19. In Figure 4.16 the red solid line defines the evolution of Fr_{t_1} with β, while the blue dashed lines enclose the transition region: being the transition gradual, we can perceive the change a little before and a little after. This lines derive from a least squares method for the Froude numbers corresponding to the transition (Fr_{t_1}), the beginning and the end of the transitional region, for each analysed β. For Froude numbers below the transition area, we obtain the wave shapes observed by Treske ([Treske, 1994]) and the field is considered one-dimensional. For Froude numbers above the transition the typical X-shape appears, changing the wave field to two-dimensional.

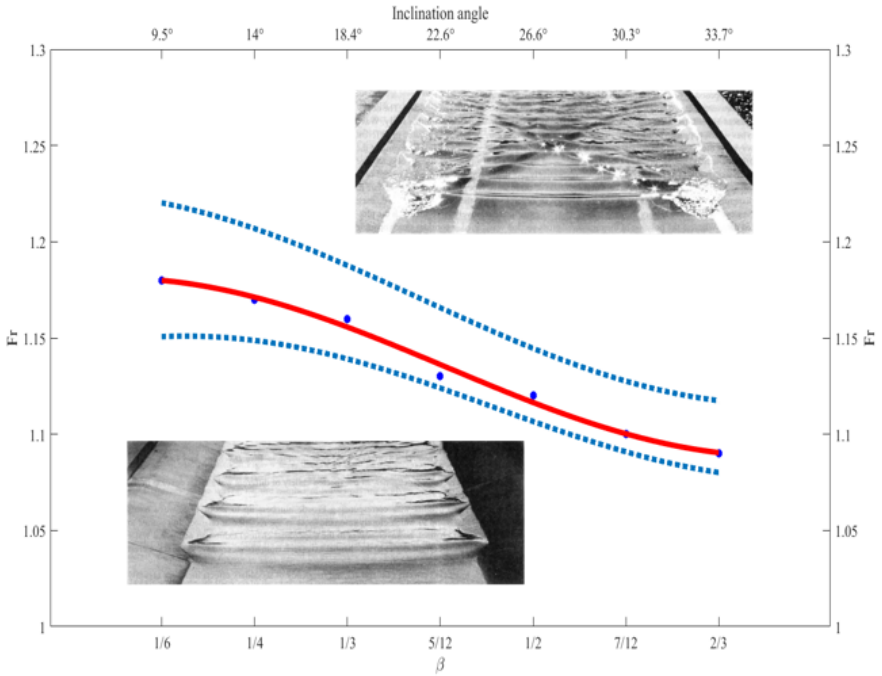

Figure 4.16 – Transition region evolving with β

We plot the relative error in the discrimination of the transition with respect to Fr_{t_1} in percentage (Figure 4.17): the maximum error doesn't exceed 6% and it is experienced for low β. The general trend is a decrease in the transition region width and thus a more evident determination of the transition with increasing β, exception made for $\beta = 2/3$, the limit case where we still perceive a transition.

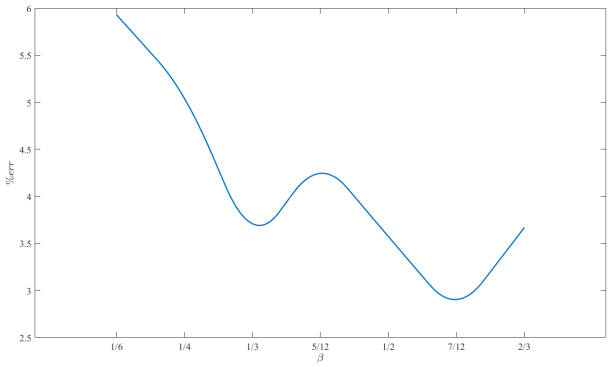

Figure 4.17 – Relative error for the individuation of the transition. The line smoothly interpolates the error of the simulation results.

From a different point of view, in Figure 4.18 we can see that the wavelength on the axis right before transition (red dotted line) becomes smaller as β increases whereas the wavelength on the banks (blue dashed line) keeps values in a small range, which is the same of the rectangular channel.

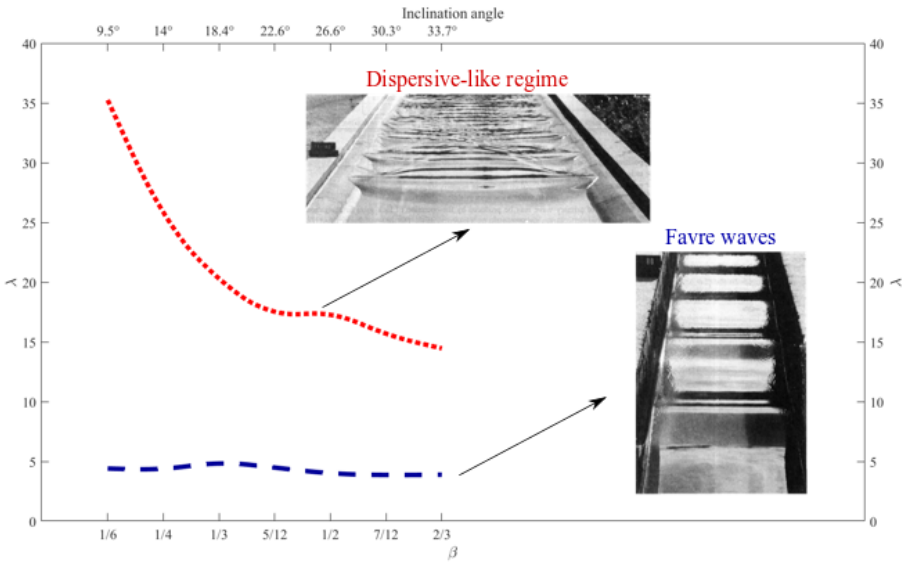

Figure 4.18 – Wavelength at transition on the axis and on the banks

Finally, combining the data of Figures 4.16 and 4.18 we can plot a "transition front"[1] linking all the points which have reached transition, before the jump in λ (Figure 4.19). This jump in the values of λ is shown with respect to the rectangular case.

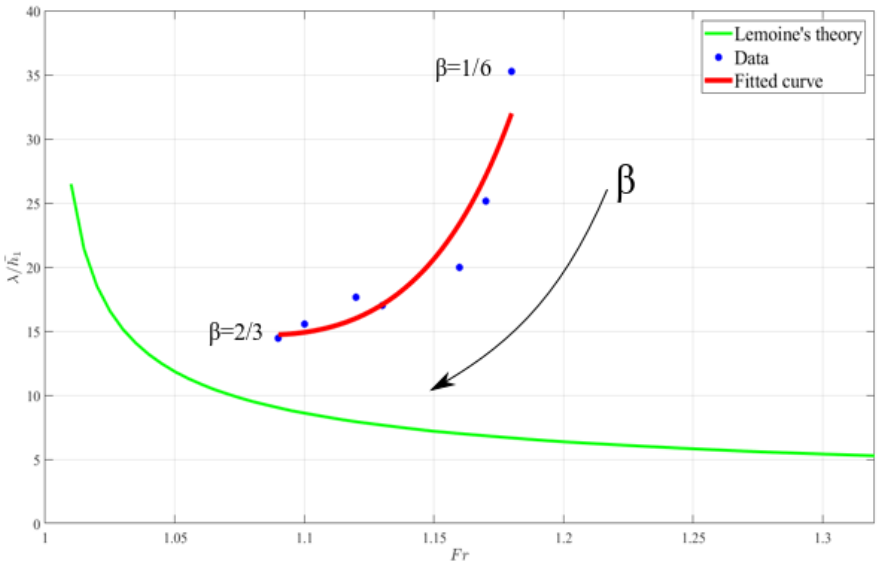

Figure 4.19 – The transition front

The results obtained with the numerical simulations can be compared with the evolution of the wavelength predicted by the linearized theory developed in [Chassagne, 2017]. In Figure 4.20, we observe that for $\beta = 1/6$ the linearized theory can well describe the wavelength evolution, unless for the values along the axis after the transition, which follow the Lemoine's theory until breaking. Some problems arise for low Froude number too, where we don't observe the expected increase in the wavelength.

[1] Here too, as for Figures 4.16 and 4.18, the lines are obtained through an approximation using a least squares method with the single cases analysed.

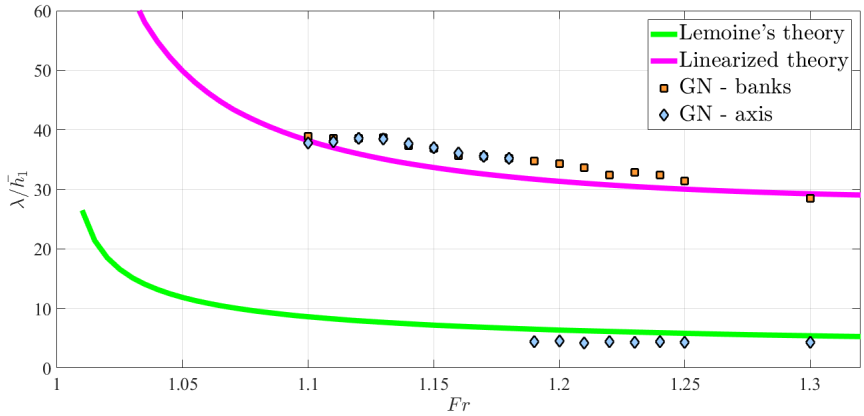

Figure 4.20 – Comparison of the simulation results with the linearized theory for a trapezoidal channel with $\beta = 1/6$

For $\beta = 1/4$ (Figure 4.21) the theory is still in good accordance with the numerical results, even though we notice a small deviation for intermediate Froude numbers.

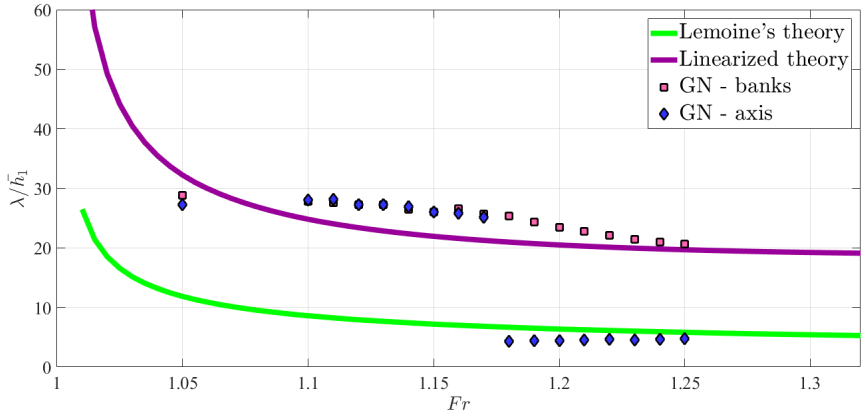

Figure 4.21 – Comparison of the simulation results with the linearized theory for a trapezoidal channel with $\beta = 1/4$

We have already seen in section 3.2 the comparison for $\beta = 1/3$ (Figure 3.12): the deviation is more important than for smaller β but still acceptable, since the numerical results fall among the experimental data. For higher β, on the other hand, the linearized theory seems to fail. There could be a non-linear mechanism caused by the refraction on the banks, which is always present but not evident for small β; when the β increases, the non-linearity becomes quite important and the deviation from the linear behaviour is non-negligible.
Indeed, this theory is linear with respect to both the flow and the geometrical variations. Thus it is appropriate for small values of β. However when the banks inclination is around 30° or higher, β can't be considered small any more and the theory is no longer valid.

These results are interesting because they point out some weaknesses of the linearized theory as it has been formulated hitherto. The numerical simulations

suggest a way to extend the linear theory to a more complete law, which takes into account also some non-linearities concerning both the flow and the geometry.

Concerning the amplitudes, we can't compare our results with theoretical or experimental data. We can only say that the transition is quite visible with the post-processing strategy used, because the high frequency amplitudes are smaller with respect to the primary waves. Changing β of course affects the evolution of the amplitudes: for small β, the secondary waves along the axis are small too because the refraction is weak; they get higher with a decreasing banks inclination. On the banks, however, the difference in the amplitudes with β is less pronounced but, in general, if the banks are very sloping, the shoaling effect is stronger and the waves are higher.

Conclusion

Ocean waves travelling into shallow water may develop into an undular bore. This dynamics is observed for rare events such as tsunamis as well as during more recurrent tidal bores or dam breaks.

Experimental measurements in estuaries and open channels ([Bonneton et al., 2015]) show a relationship between the wavelength of the undulating waves and the bore strength, represented by the Froude number. In general, the waves tend to become shorter when Fr increases. Furthermore, in the range $Fr \in [1.10\ 1.20]$, a sudden transition takes place: along the axis of the channel, the wavelength is attested to abruptly decrease, creating thus a superposition of shorter waves on the initial undular bore. This phenomenon is caused by different types of dispersive effects across the channel section. Indeed, the dynamics along the axis is governed by an intrinsic dispersion property of the flow while close to the banks the refraction of the surface waves causes a dispersive-like effect. Natural river and estuaries have such a trapezoidal-shaped bed, but manmade channels can have rectangular beds. In this case, the wavelength decreases very gently with Fr, following the theory proposed by [Lemoine, 1948]; compared to the trapezoidal case the waves are quite short, and the transition is absent.

Many depth-averaged models have been proposed to well describe the dynamics of surface waves in shallow water. The Green-Naghdi model is proven to be the most appropriate as it accounts for the non-linearity and the dispersive effects. The numerical method in the code developed in the CARDAMOM team at Inria is a hybrid model combining the GN and the NLSW models. This choice allows to take care of some lacks in the GN model, such as the simulation of the wave breaking.
The code is used in a first time to simulate the bore propagation in a rectangular and a trapezoidal channel: the results are in agreement with the experimental data ([Favre, 1935], [Treske, 1994]).

The trapezoidal channel in then analysed further, in particular the influence of the banks on the transition. To this aim, the inclination of the banks is varied in a range large enough to consider all shapes of channels, natural and artificial ones. The difference in the direction of the wave refraction caused by the differently sloped banks has an impact on the transition. In particular, for gently sloped channels, the transition takes place at relatively high Froude numbers, in the range $Fr_{t_1} \in [1.15\ 1.20]$.
Similar to Lemoine for rectangular channels, a linearized law has been proposed by [Chassagne, 2017] for the evolution of the wavelength with the Froude number in gently sloping channels. The numerical results show its validity when the inclination angle does not exceed 30°; for higher values, the non-linearity of the flow and of the geometry is non-negiglible and the theory fails.

Moreover, increasing the banks inclination causes the transition Froude number to decrease until no transition is discernible any more. In this case, the slope of the banks is too important and the effects of the refraction are too weak. Even though the waves are still slightly longer than in a rectangular channel, the dynamics can be considered the same.

The results obtained in this work suggest a possible extension of the linearized theory to a more general law if the non-linearities arising for high banks inclination are taken into account. Furthermore, as mentioned in chapter 4, we concentrated the analysis to only two non-dimensional parameters, β and Fr: one can think of a study on the influence of the channel width w/h_1 on the transition in the futur. Considering a variable bathymetry or the transportation of sediments in the numerical model would increase further the range of case studies.

The numerical simulations provide a good description of the reality and thus are of great help for the investigation of the undular bore phenomenon, since measurements in situ are usually long and difficult.

Bibliography

A. Ali and H. Kalisch. Energy balance for undular bores. *Comptes Rendus Mécanique*, 338(2):67–70, 2010.

S. Beji and K. Nadaoka. A formal derivation and numerical modelling of the improved Boussinesq equations for varying depth. *Ocean Engineering*, 23(8): 691–704, 1996.

P. Bonneton, N. Bonneton, J.-P. Parisot, and B. Castelle. Tidal bore dynamics in funnel-shaped estuaries. *Journal of Geophysical Research: Oceans*, 120(2): 923–941, 2015.

J. Boussinesq. Théorie des ondes et des remous qui se propagent le long d'un canal rectangulaire horizontal, en communiquant au liquide contenu dans ce canal des vitesses sensiblement pareilles de la surface au fond. *Journal de Mathématiques Pures et Appliquées*, pages 55–108, 1872.

K. Brauer. The Korteweg-de Vries Equation: History, exact Solutions, and graphical Representation, 2000.

R. Chassagne. Undular bore dynamics in river-like channels. Master's thesis, Ensta ParisTech, 2017.

M. Hanif Chaudhry. *Open-Channel Flow*. Springer Publishing Company, Incorporated, 2nd edition, 2007.

F. Chazel, D. Lannes, and F. Marche. Numerical Simulation of Strongly Nonlinear and Dispersive Waves Using a Green-Naghdi Model. *J. Sci. Comput.*, 48:105–116, 2011.

E. M. de Jager. On the origin of the Korteweg-de Vries equation. 2006.

H. Favre. *Étude théorique et expérimentale des ondes de translation dans les canaux découverts*. Dunod, 1935.

A. G. Filippini. *Free surface flow simulation in estuarine and coastal environments: numerical development and application on unstructured meshes*. PhD thesis, École doctorale de lathématiques et informatique, 2016.

A. G. Filippini, M. Kazolea, and M. Ricchiuto. A flexible genuinely nonlinear approach for wave propagation, breaking and runup. *Journal of Computational Physics*, 310:381–417, 2016.

S. S. Frazao and Y. Zech. Undular bores and secondary waves - Experiments and hybrid finite-volume modelling. *Journal of Hydraulic Research*, 40(1):33–43, 2002.

A. E. Green and P. M. Naghdi. A derivation of equations for wave propagation in water of variable depth. *Journal of Fluid Mechanics*, 78(2):237–246, 1976.

J. Grue, E. N. Pelinovsky, D. Fructus, T. Talipova, and C. Kharif. Formation of undular bores and solitary waves in the Strait of Malacca caused by the 26 December 2004 Indian Ocean tsunami. *Journal of Geophysical Research: Oceans*, 113(C5), 2008.

L. Holthuijsen. Waves in shallow water. In *Guide to Wave Analysis and Forecasting*, WMO - No. 702, chapter 7, pages 81–88. World Meteorogical Organization (WMO), 1998.

H. Kalisch and M. Bjørkavåg. Energy budget in a dispersive model for undular bores. *Proceedings of the Estonian Academy of Sciences*, 59(2):172, 2010.

H. Kalisch, Z. Khorsand, and D. Mitsotakis. Mechanical balance laws for fully nonlinear and weakly dispersive water waves. *Physica D: Nonlinear Phenomena*, 333:243–253, 2016.

M. Kazolea, A.I. Delis, and C.E. Synolakis. Numerical treatment of wave breaking on unstructured finite volume approximations for extended Boussinesq-type equations. *Journal of Computational Physics*, 271:281–305, 2014. ISSN 0021-9991.

A. K. Laing. An Introduction to Ocean Waves. In *Guide to Wave Analysis and Forecasting*, WMO - No. 702, chapter 1, pages 1–14. World Meteorogical Organization (WMO), 1998.

D. Lannes and F. Marche. A new class of fully nonlinear and weakly dispersive Green-Naghdi models for efficient 2D simulations. *Journal of Computational Physics*, pages 238–268, 2014.

R. Lemoine. Sur les Ondes Positives de Translation dans les Canaux et sur le Ressaut Ondulé de Faible Amplitude. (On the Positive Surges in Channels and on the Undular Jumps of Low Wave Height). *La Houille Blanche*, 2:183–185, 1948.

P. A. Madsen and O. R. Sørensen. A new form of the Boussinesq equations with improved linear dispersion characteristics. Part 2. A slowly-varying bathymetry. *Coastal Engineering*, 18(3):183–204, 1992.

O. Nwogu. Alternative Form of Boussinesq Equations for Nearshore Wave Propagation. *Journal of Waterway Port Coastal and Ocean Engineering*, 119, 1993.

D. H. Peregrine. Calculations of the development of an undular bore. *Journal of Fluid Mechanics*, 25(2):321–330, 1966.

M. Tissier, P. Bonneton, F. Marche, F. Chazel, and D. Lannes. Nearshore Dynamics of Tsunami-like Undular Bores using a Fully Nonlinear Boussinesq Model. *Journal of Coastal Research Journal of Coastal Research*, SI 64, 2011.

A. Treske. Undular bores (Favre Waves) in open channels - Experimental studies. *Journal of Hydraulic Research*, 32:355–370, 1994.

Y. Tsuji, T. Yanuma, I. Murata, and C. Fujiwara. Tsunami ascending in rivers as an undular bore. *Natural Hazards*, 4:257–266, 1991.